Chapter 5

Viscoelastic Effects during the Drainage of a Supraglacial Meltwater Lake

Meltwater lakes are seasonal features on the surface of some glaciers, appearing when there is bountiful surface melting. These lakes can reach several kilometers in diameter and can hold over one million cubic meters of water. As observed by Das et al. (2008), once these lakes begin to drain to the glacier's bed, they can drain completely over the course of a few hours. During these drainage events, the drainage rates can rival that of major waterfalls. In this work, we expand the turbulent hydraulic fracture model of Tsai and Rice (2010, 2012) to include ice viscoelasticity. We first present a direct adaptation of Tsai and Rice's semi-analytic model using an effective stress formulation for linear viscoelasticity (after Kojic and Bathe, 1987; Aagaard et al., 2011). We then use finite element models to investigate the effects of applying a more appropriate nonlinear viscoelastic ice rheology for a stationary basal crack. The solutions of the nonlinear models become increasingly similar to the linear solutions at long crack lengths, where the ice above the basal crack begins to behave in a beam-like manner. By fitting our nonlinear solutions with equivalent linear solutions at multiple crack lengths, we define an evolution law for an effective linear viscosity approximating the nonlinear viscosity. The solution for such a "pseudo-nonlinear" viscoelastic model diverges strongly from the linear models at crack lengths longer than a few ice thicknesses. However, while our models over-predict the lake drainage rates compared to observations, the impact of viscoelasticity, linear or otherwise, is at best a few percent different from comparable elastic models for rapid drainage events of supraglacial lakes with a radius of a few kilometers.

5.1 Introduction

Summer meltwater lakes are ephemeral features on the surfaces of large glaciers and ice sheets. While such lakes can grow to considerable size—up to three kilometers across and several meters deep (e.g., Das et al., 2008; Krawczynski et al., 2009)—once connected to the subglacial hydrologic network, these lakes can drain completely over the span of only a few hours. As these lakes can hold millions of cubic meters of water, the draining lake water perturbs the movement of the overriding ice during and immediately following the pulse of water reaching the glacier's base. While the impact of a single lake drainage event is short-lived, research suggests that the combined effect of a full season of lake drainages can increase the overall flow rate of glacier and may be an important process on the Greenland Ice Sheet (Zwally et al., 2002; Parizek and Alley, 2004; Bartholomew et al., 2011; Hoffman et al., 2011; Palmer et al., 2011). The supraglacial lake drainage phenomenon provides a powerful natural laboratory for investigating the link between ice deformation and basal hydrology.

A dichotomy exists in the duration of supraglacial lake drainage events. Based on field observations, the drainage can either occur slowly over many days (e.g., Raymond and Nolan, 2000) or can last only a few hours (e.g., Box and Ski, 2007; Das et al., 2008; Selmes et al., 2011). These two types drainage event occur through distinct drainage processes, such that there is not a continuum between fast and slow drainage events. Slow draining lakes use preexisting suprglacial hydrologic features (spillways, moulins, etc.) as pathways for water to reach the glacier's bed and thus also use the subglacial hydrologic system. Rapid drainage events, in contrast, commence when the weight of the supraglacial lakewater fractures the ice down to the glacier's bed, creating a conduit that drains the entire lake's volume to the bed in a few hours. Such a process will overwhelm the preexisting subglacial hydrological network.

This chapter focuses on modeling the transient behavior of the drained water upon reaching the bed of a glacier but before the fluid diffuses beneath the glacier to such an extent that the natural subglacial hydrologic network can accommodate the water. For perspective, while we focus only on the rapid lake drainage events here, the occurrence of rapid lake drainage events are somewhat rare, ranging from less than 1% to 25% of all lake drainage events across Greenland, depending on the region studied (Selmes et al., 2011).

The observation motivating this work is a meltwater lake drainage event observed by Dal et al. (2008) on the Greenland Ice Sheet near Jakobshavn Isbrae in July of 2006. This event represented the best observed event to date. Over the month of July, a meltwater lake with a volume of about 4.4e7 m^3 of water formed on the glacier's surface. This lake proceeded to drain completely into the ice sheet in less than 1.5 hours, causing about a meter of uplift and lateral translation at a GPS monitoring station located 1.7 kilometers away from the main drainage conduit. Shortly after the lake finished draining, the displacement signal began to decay from its peak value and fell to a constant offset from the original position after about 2.5 hours. Prior to drainage, a crack about 3 kilometers long and 0.5 meters wide appeared near the lake, suggesting that this crack may have triggered the drainage event by connecting the lake to the subglacial hydrologic network.

To date, the mathematical modeling of these drainage events is somewhat limited. Most models focus on the conditions necessary to drive a pulse of surface water to the bed of the ice sheet (e.g., Alley et al., 2005; Krawczynski et al., 2009) or the conditions within the supraglacial lake (e.g., Tedesco et al., 2012), rather than investigating the diffusion of the fluid beneath the ice sheet once the water reaches the bed. Tsai and Rice (2010, 2012) model the drainage of the lake as a fluid-filled crack propagating horizontally along the base of an elastic ice sheet. The models of Tsai and Rice predict that a sizeable basal crack (5-10 kilometers in length) is necessary to accommodate the draining water, but are unable to accurately match the magnitude of the observed surface displacement from Das et al. (2008).

While viscoelasticity has not been investigated for the lake drainage problem, the research discussed in the previous chapters suggests that viscoelasticity may be important during processes on hourly to weekly timescales. For example, viscoelasticity has been cited as a necessity in the modeling of the tidal loading of Antarctic ice streams (e.g., Anandakrishnan and Alley, 1997; Gudmundsson 2006; 2007; 2011; Walker et al., 2012) and our own work has demonstrated that viscoelasticity is important for determining the timing of an ice stream's response to a tidal load. Despite the timescale for lake drainage being only about two hours, we find a Maxwell relaxation time of similar magnitude for our loading stresses of approximately 10^6 Pa ($\tau_{max} = \frac{\eta_{eff}}{E} \approx 10^2 - 10^3$s). As the

Maxwell relaxation time is within a few orders of magnitude of the duration of lake drainage events, we expect measureable viscoelastic effects during such drainage events.

We present results from both linear and nonlinear viscoelastic modeling of the drainage of a supraglacial lake, using the hydraulic crack propagation model of Tsai and Rice (2012) as the basis for our work. We modify the model of Tsai and Rice (2012) using an effective stress formulation for linear viscoelasticity after Kojic and Bathe (1987) and Aagaard et al. (2011). We then compare these linear results to equivalent finite element models using nonlinear viscoelasticity, finding that these nonlinear solutions can be approximated using a variable (effective) linear viscosity. We end with a comparison of our model results to the field observations of the July 2006 lake drainage event observed by Das et al. (2008).

5.2 Model Methodology

This section discusses the model methodology used throughout this chapter. The opening subsection begins with a discussion of the approach of Tsai and Rice (2010; 2012) for modeling the opening of a crack at the base of a glacier that is filled with a turbulent fluid. Additionally, we highlight the modifications necessary to apply a linear viscoelastic rheology to the material surrounding the crack. In the next subsection, we discuss the hybrid Chebyshev/series minimization method used to find our model solutions. The methods section closes with a discussion of the finite element models used to explore the importance of using a nonlinear viscoelastic rheology for ice.

5.2.1 General Model for Turbulent Hydraulic Fracture

We model the supraglacial lake drainage system as a two-dimensional water-filled crack of length *2L* at the base of an impermeable viscoelastic (ice) body of thickness *H* above a similarly viscoelastic half-space, as shown in figure 5.1A. The crack grows as a function of time, as long as the fluid pressure at the drainage conduit is greater than the hydrostatic overburden pressure in the basal conduit. Our model unknowns are the crack opening (w), the excess fluid pressure compared to overburden pressure (p), and the fluid velocity (U) that satisfy the appropriate fluid flow, conservation, fracture, and rheological equations. As previously mentioned, our methodology only varies from Tsai and Rice (2012) in our choice of rheology.

The Reynold's number of the fluid flow in our model is Re $\approx 10^6 m^{-1} \cdot L$, suggesting turbulent flow in cracks longer than ~ 10 cm. As we expect a much longer basal crack, we adopt the turbulent flow model of Manning and Strickler (Manning, 1891; Strickler, 1923; Strickler, 1981) using the Darcy-Weisbach friction factor of $f = f_0(k/w)^{1/3}$ where f_0 is a reference value of f and k is the Nikuradse roughness height (Rubin and Atkinson, 2001; Gioia and Chakraborty, 2006; Tsai and Rice, 2010; 2012). The resulting fluid flow relationship is:

$$-\frac{\partial P}{dx} = \begin{cases} -\dfrac{f_0 \rho U^2}{4}\dfrac{k^{1/3}}{w^{4/3}} & \text{for } x > 0 \\ \dfrac{f_0 \rho U^2}{4}\dfrac{k^{1/3}}{w^{4/3}} & \text{for } x < 0 \end{cases} \tag{5.1}$$

where ρ is the fluid density and x is the horizontal dimension. The conservation of mass for an incompressible fluid, when applied within the basal crack, requires:

$$\frac{\partial wU}{\partial t} + \frac{\partial w}{\partial t} = 0 \tag{5.2}$$

For the growth of our mode I crack, we assume the fracture criterion to be:

$$K_I = K_{IC} = 0 \tag{5.3}$$

Justification for setting the critical fracture intensity equal to zero is provided in Tsai and Rice (2010; 2012).

For our rheological law, we use the effective stress formulation for linear viscoelasticity (Kojic and Bathe,1987; and Aagaard et al., 2011; see Appendix 5A) to modify the elasticity equations of Erdogan et al. (1973). This new viscoelastic rheological relationship is:

$$0 = -\sigma_{XZ} = \int_{-L}^{L} \left[\left(\frac{1}{s-x} + k_{11} \right) \frac{\partial u}{\partial s} + k_{12} \frac{\partial w}{\partial s} \right] ds \tag{5.4A}$$

And

$$-4\pi p(x) S_{VE} = \int_{-L}^{L} \left[k_{21} \frac{\partial u}{\partial s} + \left(\frac{1}{s-x} + k_{22} \right) \frac{\partial w}{\partial s} \right] ds \tag{5.4B}$$

where σ_{XZ} is the two-dimensional shear stress, S_{VE} is the vertical normal component of the consistent viscoelastic tangent compliance modulus (fully defined in appendix 5A), and the k_{ij}'s are coefficients taken from Erdogan et al. (1973).

The initial and boundary conditions used to close these four equations are:

$$\begin{gathered} p(0,t) = p_I \\ w(L,t) = 0 \\ U(L,t) = U_{tip} = \frac{dL}{dt} \end{gathered} \tag{5.5}$$

where p_I is the inlet pressure at the conduit base and U_{tip} is the fluid velocity at the crack tip. These three conditions ensure that the pressure at the center of the crack is held constant (and is assumed to be equal to the weight of the water in the conduit minus the ice overburden pressure), the crack is closed at and beyond the crack tip, and that the fluid motion at the crack tip is the same as the propagation velocity of the crack tip itself, such that there is always fluid in the crack tip region. Later in this chapter, the value of the pressure at the crack center will be modified to reflect the variability of the inlet pressure as a function of conduit size and fluid height.

5.2.2 Solution Method

To solve the conservation equations, we use the hybrid Chebyshev/series-minimization scheme detailed in Tsai and Rice (2012). First, the conservation equations are non-dimensionalized using the relations shown in Table 5.1. We then take $\hat{p}(\hat{x},\hat{t})$ and $\widehat{w}(\hat{x},\hat{t})$ as:

$$\frac{\hat{p}(\hat{x},\hat{t})}{D} = \sum_{k=0}^{2N} a_k p_k(\hat{x}) = a_0 p_0(\hat{x}) + \sum_{k=1}^{N} a_{2k-1}[c_{2k-1} - |\hat{x}|^{2k-1}] + \sum_{k=1}^{N} a_{2k}[c_{2k} - U_{2k}(\hat{x})] \tag{5.6}$$

and

$$\frac{\widehat{w}(\hat{x},\hat{t})}{D} = \sum_{k=0}^{2N} a_k w_k(\hat{x}) = a_0\left(\frac{1-\hat{x}}{2}\right)^{6/7} + \sum_{k=1}^{2N} a_k w_k(\hat{x}) \tag{5.7}$$

where U_{2k} are Chebyshev polynomials of the second kind; c_k and D are fitted parameters such that w_k and p_k satisfy equations 5.3 and 5.4; and a_k will be solved for later. Note that our formulation of viscoelasticity requires a modification to Tsai and Rice's fitting method for the parameters c_k and *D*. To account for the time-variable effective Young's modulus introduced by our viscoelasticity model, the force component F_{21} of equation 7.100 in Erdogan et al. (1973) is set equal:

$$
\begin{aligned}
&F_{21} = -\frac{\pi}{2} p_I S_{VE} && \text{dimensional} \\
&\hat{F}_{21} = -\frac{\pi}{2} \hat{S}_{VE} && \text{non-dimensional}
\end{aligned}
\tag{5.8}
$$

Propagating this change through all our equations, we now solve for the coefficients c_k and *D* and then combine equations 5.1 and 5.2 using an implicit (backwards Euler) scheme to approximate the time derivative of *w*, such that :

$$
\frac{-(\sum_k a_k w_k)^{10/3}}{{a_0}^{4/3}/7} \frac{\partial(\sum_k a_k p_k)}{\partial \hat{x}}\Bigg|_{t_1} = \left[\int_{\hat{x}}^{1} \frac{\sum_k a_k w_k|_{t_1} - \sum_k a_k w_k|_{t_0}}{\hat{t}_1 - \hat{t}_0}\right] \tag{5.9}
$$

where t_0 is the current timestep and t_1 is the next timestep. Note that the initial solution is found using the self-similar solution of Tsai and Rice (2010). Equation 5.9 satisfies the fluid flow requirements within the crack as the crack lengthens as a function of time. This equation closes the system of equations necessary to solve for the coefficients a_k that minimize the error between the two sides of this equation, under the added constrain that $\hat{w}(\hat{x}, \hat{t})$ must remain nonnegative. A variable timestep is chosen to be equal to the time required for the crack length to change by 5%.

To determine the impact of viscoelasticity on our model's solution, we compare our viscoelastic results to those found using the purely elastic rheology of Tsai and Rice (2012). We note that at each timestep, the value of S_{VE} changes and thus the ratio of viscous to elastic deformation changes. The variability in S_{VE} implies that the final result must be found by iteratively changing the crack length. The derivation of S_{VE} and its physical interpretation are discussed in appendix 5A.

5.2.3 Nonlinear Viscoelasticity and Finite Element Implementation

Ice is traditionally modeled using the nonlinear Glen flow equation (Glen, 1955; 1958) for viscous deformation, rather than the Newtonian fluid equation discussed and implemented above. Unfortunately, though an equivalent stress form of a nonlinear viscoelastic material exists (e.g., Kojic and Bathe, 1987; Aagaard et al., 2011), such a formulation cannot be used to represent ice in our semi-analytic model as S_{VE} would be a function of *p(x)* and thus *x*. The field equations from which we derive our equation 4 require the separation of the material moduli from the spatial derivatives of the displacements (see Erdogan and Gupta, 1971), such that a problem with spatial variable moduli cannot be solved explicitly in our current framework. Thus, we use to a finite element version of our analytic models to explore the impact of using a more physically representative nonlinear viscoelastic rheology for ice.

We use the program *PyLith* for our finite element analysis (Williams et al., 2005; Williams, 2006; Aagaard et al., 2007; 2008). Figure 5.1B shows a schematic of our finite element version of the lake drainage problem. Only half of the crack (length-wise) is modeled due to the symmetry across the crack's central axis. The ice body has a domain above the crack of thickness *H=1 km*, a domain below the crack with a thickness much greater than *H* to approximate a half-space, and a region of uncracked ice at least *5L* long. To define unique upper and lower surfaces of our crack, an offset Δh separates the two edges, where $\Delta h \ll w$. These models use a three-dimensional "pseudo-plane-strain" mesh, where there is a finite thickness in the third dimension but the displacements in this direction are set equal to zero. This approach is equivalent to assuming the problem is infinite in the third dimension.

In our finite element analysis, we do not iteratively lengthen our crack, but instead use a crack of known length and a pressure distribution taken from our linear viscoelastic results to determine what the expected nonlinear viscoelastic crack opening would be. Thus, the fluid equations (equations 5.1 and 5.2) are not satisfied for this static finite element formulation of the viscoelastic model, as the value of w increases with time. However, where the viscous crack opening is small compared to the elastic crack opening, the effect on the overall surface deformation of not accounting for the time-dependent viscous opening on the pressure distribution is negligible.

The total model time is equal to the timestep in the linear viscoelastic model at the same crack length. Note that while the timestep varies slightly with varying viscosity in the linear model, all timesteps are chosen from the model with $\eta = 1e11\ Pa \cdot s$. For the models shown here, the model-averaged error in the speed of crack propagation introduced by using the timestep calibrated to a single linear rheology can be as high as 5%, with increasing errors for models with viscosities increasingly different from our reference model. Such an error is deemed acceptable, as an iterative scheme coupling the fluid flow, mass conservation, and fracture equations to the finite element model output for a nonlinear rheological model is beyond the scope of this work.

The applied boundary conditions in the finite element model are equivalent to those used in the analytic model with a few extra conditions where required by the finite element method. Along the crack of length L, the pressure distribution $p(x \geq 0)$ from the linear viscoelastic model of the same crack length is applied to both sides of our crack as a normal traction. The nodes at (and beyond) the crack tip are held to have zero displacements in all directions. We ensure the symmetry of our solution by fixing u along the nodes above and below the center of the crack. The base of the half-space domain is held fixed, with zero displacements in all directions.

5.3 Model Solutions

In this section, we present solutions from our semi-analytic linear viscoelastic models and from our finite element nonlinear viscoelastic models. The first subsection summarizes the linear viscoelastic model results, focusing on the relative importance of the viscous component of deformation over the evolution of the drainage crack. The second portion of this section discusses the results of our nonlinear models, comparing these nonlinear results to the linear model output. Lastly, the final subsection describes a method for approximating the nonlinear viscoelastic behavior of ice using a time-variable viscosity in our linear semi-analytic model.

5.3.1 Linear Viscoelastic Results

The motivation behind implementing a linear viscoelastic rheology is to quantify the variation between the viscoelastic and elastic solutions to our lake drainage model, and to determine if using a viscoelastic model is necessary to reproduce the Greenland observations. Our model explored a range of viscosities between $\eta = 1e12\ \mathrm{Pa \cdot s}$ and $1e11\ \mathrm{Pa} \cdot s$, as these bracket the magnitude of the nonlinear crack openings discussed in the next section (5.3.2). For comparison, such viscosities also match the range of published linear viscosities for ice under similar strain-rates and stresses (e.g., Jellinek and Brill, 1956; Reeh et al., 2003). Note that only the most representative model results are plotted here and that the figures discussed in this section also have results for our "pseudo-nonlinear" model, which will be discussed later in section 5.3.3.

Figure 5.2A shows the dimensionless pressure and crack opening at several crack lengths for the elastic and end-member viscoelastic models. Only at the longest crack length (*L/H=5*) do any noticeable variations in pressure exist between the models, though even at *L/H=5* the difference between models is modest. For the dimensionless crack opening (figure 5.2B), there are substantial deviations between the elastic and viscoelastic solutions starting at a crack lengths of *L/H>1*, with even a slight variation as early as a crack length of *L/H=0.5*.

These snapshots of $\hat{w}$ suggest that the viscous deformation becomes more important as the crack length increases. To further explore this effect, figure 5.3A compares the time rate of change of the crack opening for a viscoelastic ($\eta = 1e12\ Pa \cdot s$) and an elastic model and figure 5.3B shows the elastic and viscoelastic deformation for these models as functions of crack length. Both the elastic and viscoelastic models predict increasing deformation rates with increasing crack length, but the viscoelastic model predicts a higher rate of deformation than is seen in the elastic model. Thus, as the basal crack grows, there should be an increase in the relative amount of viscous crack opening.

Lastly, the scaled velocity $\phi = \frac{U_{TIP}}{U_S}$ increases at longer crack lengths compared to the expected rate from the $L^{1/6}$ dependence of U_S alone (see Figure 5.4). At a crack length of L/H=5, the value of the scaled velocity is about 6 times the scaled velocity at a crack length of L/H=0.02. This strong dependence of ϕ on crack length was first reported by Tsai and Rice (2012). Our results demonstrate that viscoelasticity further increases the dependence of the scaled velocity on the crack length. Additionally, decreasing the viscosity in the viscoelastic model increases the value of ϕ at a given crack length. The inset portion of figure 5.4 shows the expected variation between the viscoelastic and elastic solutions to longer crack lengths. As with the crack opening, the relative difference between solutions increases over crack lengths of interest, though the relative crack velocity does asymptotically approach a constant value at very long and very short crack lengths.

In summary, our linear viscoelastic models predict increased crack opening, crack opening rates, and crack propagation speeds than the elastic model. The differences between the two rheologies become important at a crack length roughly equivalent to the ice sheet thickness, with viscoelasticity becoming increasingly important at longer cracks.

5.3.2 Nonlinear Viscoelastic Results

Having demonstrated that the viscoelastic solution deviates from the elastic solution, especially for crack lengths that approach and surpass the thickness of the upper ice layer, we now explore the importance of using a more physically representative stress-dependent viscosity as the viscous portion of our ice rheology. We compare the linear viscoelastic solutions just discussed to the solutions from our nonlinear viscoelastic finite element models, using a reference viscosity coefficient for our glacier corresponding to a uniform temperature of -5°C (taken from Cuffey and Paterson, 2010). Recall our nonlinear models do not change the pressure or crack length, but rather model a single chosen crack length and timespan equivalent to the linear viscoelastic model. Thus, the greater the variation between the nonlinear and linear models, the more important using nonlinear viscoelasticity is to correctly model the ice deformation.

Figure 5.5 shows the nonlinear viscous crack opening at four different crack lengths (20 meters, 1 kilometer, 2 kilometers, and 3.333 kilometers) plotted against the linear viscous crack openings for a range of linear viscosities. Two features are immediately apparent: the relative magnitude of the nonlinear model compared to the linear models varies in time, and the character of the nonlinear crack opening changes with increasing crack length. This second feature is confirmed in the upper panels of figure 5.6, which show the normalized linear and nonlinear crack openings and the normalized pressure. The lower panels in figure 5.6 plot the effective viscosity of the upper and lower crack surfaces. The effective viscosity is defined in appendix 5C.

As the crack grows longer, the magnitude of viscous deformation increases in relation to the magnitude of the elastic deformation, as is expected from our linear viscous elastic modeling. Such a trend is shown in figure 5.7A. Note that while the viscous deformation monotonically increases, the trend in the exact value is not constant. The relative viscous deformation grows very rapidly around $L/H=0.02$, slows at $L/H\approx 0.025$ and then speeds up after $L/H\approx 1$. Figure 5.7B shows the relative viscous deformation in the upper crack edge compared to the lower crack edge. With increasing crack length, the viscous deformation of the upper crack edge rapidly grows large enough to dominate the overall viscous crack opening signal. The upward partitioning of the viscous deformation is especially pronounced beyond *L/H≈0.5*, and is caused by the reduced effective viscosity in the upper body at longer crack lengths (see appendix 5C).

From these features, the nonlinear crack growth is divided into three regimes as a function of *L/H*: a half-space regime for short cracks (*L<< H*), a beam-like regime for long cracks (*L>H*), and a transitional regime in between (*L≈H*). The remainder of this section discusses each of these regimes in turn. The transitional region is defined on the lower end by the location where the trend in $\frac{w_V}{w_E}$ changes slope (figure 5.7A) and on the upper end by the region where the normalized viscous deformation coincides with the normalized linear deformation (figure 5.6). The domain of each regime is shown in figure 5.7.

5.3.2.1 Half-Space Regime

At the shortest crack length, the deformation within the finite-thickness upper ice layer and the lower half-space are effectively indistinguishable. Using figure 5.6A as a representative model within this crack regime (appropriate as L is 20 times smaller than *H*), the nonlinear solution clearly deviates greatly from the linear solution. The nonlinear model predicts that the viscous deformation should be more uniform along the crack length than in the linear model. This is equally evident in figure 5.5A, where near the crack tip, the nonlinear solution predicts a deformation of similar magnitude to the linear model with a viscosity of $1e11\ Pa \cdot s$, while near the crack center, the solution approaches that of a linear model with a viscosity of $1e12\ Pa \cdot s$. Additionally, a region of increased deformation exists at the crack tip, unlike the linear viscoelastic trend of monotonically reduced crack opening along the crack length.

As seen in figure 5.6A, the effective viscosities in the upper and lower halves of the models are essentially the same. As the effective viscosity is stress dependent, an equal effective viscosity implies that the stress induced by the fluid pressure in the crack is evenly partitioned between the upper and lower model regions. As expected, the changes in effective viscosity along the length of the crack mirror the value of the fluid pressure in the crack, and the region of highest effective viscosity corresponds to the zero crossing of the relative pressure. Near the crack tip, the large negative pressures (i.e., excess ice overburden pressure) cause a drop in the effective viscosity. This reduced viscosity creates the region of increased deformation seen at the crack tip.

Finally, while the crack opening is equal in the upper and lower portions of the crack, the overall magnitude of the crack deformation at this short crack length is very small compared to the elastic deformation (figure 5.7). In this half-space regime of crack growth, the relative viscous deformation is substantially less than 1% of the elastic opening. Thus, for cracks short enough to be in the half-space regime, modeling viscoelasticity is unnecessary as the viscous deformation is trivial.

5.3.2.2 Transitional Regime

As the basal crack increases in length, the profile of the crack opening changes. When the crack length approaches the ice thickness, the free surface begins to impact the deformation of the top edge of the crack. Eventually, the nature of the crack opening transitions from the half-space regime discussed above to the beam-like regime that will be discussed in section 5.3.2.3. Within the transitional regime between the half-space and beam-like regimes, the crack opening near the center of the crack ($\hat{x} \approx 0$) increases relative to the crack opening near the crack tip. In the normalized crack opening figures (upper panels of figure 5.6), such a trend manifests itself as a convergence towards the linear viscoelastic solution as the crack lengthens. The solution completely transitions into the beam-like regime when the normalized difference (R^2 value) between the linear and nonlinear crack openings drops below 10%.

The explanation for the nonlinear model's trend towards the linear solution with increased crack length, is tied to both the increasingly beam-like nature of the upper ice body and the larger magnitude of the crack opening for longer cracks. The combined effect of these factors is that the effective viscosity within the upper body steadily decreases as the flexural (bending) stresses within the upper body become more pronounced. This understanding is built upon five modeling results:

1) As demonstrated in appendix 5B, the normalized bending shape of a beam is somewhat insensitive to the nature of an applied pressure distribution as long as the pressure is roughly the same near the free edge of the beam.

2) In our nonlinear models with L/H>~1, the flexural stress (i.e., the stress proportional to $\frac{\partial^2 w}{dx^2}$) in the upper ice body is larger than the stress induced in the body by the applied pressure. Furthermore, the opening increases faster than linearly with increasing crack length (figure 5.3), implying that this flexural stress becomes increasingly more dominant than the (roughly constant) applied pressure at larger crack lengths.

3) As the stress in the upper ice body is dominated by the flexural stress, the effective viscosity can be approximated by the flexural stresses independent of the applied pressure. Such a result is seen in the bottom panels of figure 5.6, where the effective viscosity of the upper body (blue) diverges from the effective viscosity of the lower body (red) at increasing crack length.

4) For L/H>~1, the flexural stress is close to uniform save near the middle of the beam, where the stress is low. Therefore, the effective viscosity only changes significantly near the middle of the upper ice body, where the effective viscosity is high.

5) As demonstrated in appendix 5B, the normalized bending profile of a beam is insensitive to changes in the material parameters near the middle of the beam. Thus, the nonlinear crack model begins to behave more like the linear crack model as the crack grows longer.

However, within the entire transitional regime, the viscous crack opening is less than 10% of the elastic opening, suggesting that viscoelasticity is still somewhat negligible even as the upper ice body begins to act more beam-like.

5.3.2.3 Beam-Like Regime

Once the crack grows to $L/H \approx 2$, the normalized nonlinear viscous deformation is only slightly different from the linear viscoelastic deformation for the reasons discussed above. However, while the normalized solution may be well approximated using a linear effective viscosity, the value of the nonlinear crack opening increases such that the viscosity of an equivalent linear model drops with increasing crack length. An appropriate equivalent effective viscosity, $\tilde{\eta}_{eff}$, for the nonlinear model at a given crack length is found by fitting the nonlinear solution to a series of linear viscoelastic models over a range of viscosities. Figure 5.8 shows the trend in these equivalent effective viscosities, $\tilde{\eta}_{eff}$, as a function of crack length, for cracks within the beam-like regime.

As in the transitional regime, the reason for the decrease in $\tilde{\eta}_{eff}$ with crack length is the increased crack opening at longer crack lengths. The larger crack opening leads to larger flexural stresses that in turn result in the reduced equivalent effective viscosity around the crack center and tip. While the fitted value of $\tilde{\eta}_{eff}$ falls between the maximum and minimum values of effective viscosity in the material immediately above the crack, $\tilde{\eta}_{eff}$ does not correspond to any standard statistical measure of the effective viscosity. Both the median and mean values of the effective viscosity overestimate the value of $\tilde{\eta}_{eff}$ for the corresponding linear viscoelastic model. Thus, we rely on an empirical relationship for $\tilde{\eta}_{eff}$, finding that the evolution of $\tilde{\eta}_{eff}$ with crack length can be well fit using:

$$\log_{10}(\tilde{\eta}_{eff}) = 12.72 - 0.37L \tag{5.10}$$

Lastly, the magnitude of the viscous deformation becomes a substantial fraction of the elastic deformation in the beam-like regime, reaching a 1:1 ratio between the viscous and elastic deformation at a crack length just over *L/H≈5*. Thus, once the crack has grown to several times the ice thickness, the viscous deformation becomes as important as the elastic deformation. For cracks of the length predicted by Tsai and Rice

(2010; 2012), the viscous deformation should surpasses the elastic deformation late in the crack evolution.

5.3.3 "Pseudo-Nonlinear" Viscoelastic Results

From the nonlinear results presented above, the nonlinear viscoelastic solution only varies significantly from the linear solution when the overall viscous deformation is negligible. As such, the nonlinear viscoelastic deformation can be approximated by using the linear viscoelastic semi-analytic model with a time-varying (i.e., crack length dependent) equivalent effective viscosity. The evolution of the equivalent effective viscosity is fit empirically using equation 5.10. We call this model our "pseudo-nonlinear" (PNL) model.

Returning to figures 5.2 to 5.4, the PNL solution is the black curve in all three figures. As with the linear viscoelastic model, the PNL pressure solution, shown in figure 5.2A, only differs slightly from the other model pressure distributions, even at a crack length of *L/H=5*. The total crack opening of the PNL model is smaller than that of the linear viscoelastic model with a viscosity of $1e11$ Pa · s at crack lengths up to and including *L/H=1* (figure 5.2B). This result is expected as the equivalent effective viscosity in the PNL model is greater than that of the shown linear viscoelastic model at these crack lengths. At *L/H=5*, the crack opening in the PNL model surpasses that of the linear model with a viscosity of $1e11$ Pa · s, despite only having a lower effective viscosity at crack lengths greater than *L/H=~4.7*. Such behavior is easily explained by the rapid change in $\frac{d\hat{w}_v}{dt}$ in figure 5.3A, as the decreasing effective viscosity at larger crack lengths further enhances the viscous opening rate beyond that seen in the linear model. Similarly, in figure 5.4, the scaled fluid velocity increases faster in the PNL model than in either the elastic or linear viscoelastic models.

Given the well-established nonlinearity of the viscous deformation of ice, our PNL model is the most physically representative model for crack propagation considered here. However, a major assumption of the PNL approach is that the input pressure remains constant, as our empirical fit of the nonlinear effective viscosity (equation 5.10) holds only for a constant inlet pressure. Calibrating an empirical fit that allows for variable pressure would necessitate knowing the pressure history, which would require a full crack evolution model to determine consistent values of crack opening, crack propagation velocity, and inlet pressure. Such modeling is well beyond the scope of this work. Thus, the PNL solution is presented as an indication of the expected results for a nonlinear viscoelastic model, but as will be discussed in the next section, the need for a variable inlet pressure when modeling the Greenland observations dictates our decision to directly compare only the observations to our the linear model results.

5.4 Comparison to Observations

The model results discussed in the previous sections demonstrate that viscoelasticity becomes increasingly important as the basal crack grows longer. We now compare the linear model results to the observations of Das et al. (2008) to determine if viscoelasticity is an important consideration for realistic lake drainage problems. First, we use our models to predict the drainage rate and volume of a theoretical supraglacial lake, comparing the drainage times of our models to observations of lake level height during the Greenland lake drainage event. Second, we create a finite element model to determine the expected surface deformation during and immediately following a lake drainage event, comparing our model results to a GPS station placed by Das et al. (2008) 1.7 kilometers away from the drainage conduit during the Greenland event.

5.4.1 Lake Drainage

Das et al. (2008) observed a lake of volume 0.044 km^3 of water drained from the surface completely in less than two hours. We create a simple model for the volume in the lake, conduit, and crack system by assuming that the surface lake has a constant cross-sectional area of 5.6 km^2 (as reported by Das et al. 2008), the basal crack volume is approximated as a cylinder of with height equal to an average crack opening, and the drainage conduit is an oblong cylinder of semi-major axes a and $u_0 = a\frac{p_I}{2E}$, and height H. The resulting drained volume is:

$$V_d = V_b + V_c \approx \pi L^2 w_{ave} + \frac{\pi a^2 H p_I}{2E} \tag{5.11}$$

This geometry is shown schematically in figure 5.9. Two implicit assumptions of this model are that while the lake is draining, no water leaves the crack system and that there is a constant input pressure at the intersection of the drainage conduit and the basal crack during the initial drainage phase. However, once the finite volume of the lake drains ($V_d = V_0$), the water level in the conduit will begin to drop due to the conservation of volume in the conduit/crack system. The height of the water level in the conduit system, H_W, during the post-drainage phase is defined to be (after Tsai and Rice, 2010):

$$H_W = H\left(\frac{\rho_{ice}}{\rho} + \frac{\rho_{ice} - \rho}{\rho}\chi_w\right) \tag{5.12}$$

where χ_w is a constant between 0 and 1. As the inlet pressure is linear with water level, we make the substitution:

$$p_I = \chi_w p_{static} \tag{5.13}$$

where p_{static} is the overburden pressure of a static water column of height H. The value of χ_w can now be found by substituting $w_{ave} = \frac{\hat{w}_{ave} p_I L}{E}$, $V_d = V_0$, and equation 5.13 into equation 5.11, resulting in:

$$\chi_w = \frac{L\hat{w}_{ave} - \frac{H\rho_{ice}}{\rho}\left(\frac{a}{L}\right)^2 \pm \sqrt{\left(\frac{H\rho_{ice}}{\rho}\left(\frac{a}{L}\right)^2 - L\hat{w}_{ave}\right)^2 - 2\frac{\rho_{ice}-\rho}{\rho}\left(\frac{a}{L}\right)^2 \frac{V_0 E}{\pi L^2 p_{static}}}}{\frac{H\rho_{ice}}{\rho}\left(\frac{a}{L}\right)^2} \tag{5.14}$$

In this form, the only quantity other than χ_w that is unknown is $\left(\frac{a}{L}\right)$, the ratio of the conduit's long axis to the length of the basal crack. As discussed in Tsai and Rice (2010; 2012), we expect $\left(\frac{a}{L}\right)$ to be between ~ 0.1 and 1.0. As our bias is towards larger values of $\left(\frac{a}{L}\right)$ due to the sizable crack observed by Das et al. (2008), we impose a range of values for $\left(\frac{a}{L}\right)$ equal to 0.7, 0.8, 0.9, and 1.0, allowing us to solve explicitly for the drainage volume.

Figure 5.10 shows the drainage volume, drainage rate, and crack opening for these four models. The elastic model solution is shown in blue, while the solution to the linear viscoelastic model with a viscosity of $\eta = 1e11$ Pa · s is in red. As will be discussed later, this viscosity provides an overestimate of the viscous deformation for an equivalent PNL version of this analysis (see subsection 5.5.2).

From figure 5.10, our model predicts more rapid drainage than the Greenland observations suggest, with the total lake volume draining into the conduit in only ~ 0.32

hours. As expected from this exceedingly short duration, the drainage rates are about 20 times larger than the peak observed drainage rate of ~ 14,300 m^3/s. Note that this drainage rate is the linear drainage rate between the final two undrained lake level measurements of Das et al. (2008), assuming a constant lake area. Additionally, varying the values of $\left(\frac{a}{L}\right)$ makes essentially no difference for the model's solutions. For example, the largest difference in drainage time is about 0.2% and the greatest difference in peak crack opening is about 2% between all values of $\left(\frac{a}{L}\right)$. This near-independence of the solution on $\left(\frac{a}{L}\right)$ implies that the basal crack volume, rather than the conduit's volume, controls the total drainage volume, and that the dependence of χ_w on $\left(\frac{a}{L}\right)$ is minimal.

Comparing our elastic (blue lines) and viscoelastic models (red lines), the viscoelastic solution completely drains the supraglacial lake faster than the elastic solution, as expected from to the added viscous component of deformation. The difference in drainage time between the solutions is 0.0065 hours (23.4 seconds), a difference of about 2%. However, the difference in the modeled crack opening is more pronounced, with the viscoelastic solution predicting a crack opening about 9% larger than the elastic model. Additionally, after the lake has finished draining, the difference in the modeled crack openings grows, reaching a difference of about 17% between rheologies two hours after the lake drainage began. The exception to this trend is the brief period of time where elastic crack is growing while the viscoelastic crack is shrinking. Thus, the viscoelastic model predicts slightly faster lake drainage, a larger peak crack opening value, and larger crack openings during the post-drainage phase.

To address our exceedingly rapid lake drainage, we now apply a correction for the fluid drag on the water falling through the vertical conduit. Following appendix D of Tsai and Rice (2010), the conduit size dictates the turbulent loss of fluid pressure. This effect is added to our models by introducing a correction factor χ to the pressure term, where χ is constant between 0 and 1 representing the fraction of total fluid overburden pressure transmitted to the basal crack. The relationship between χ, L, and a, taken from equation D12 of Tsai and Rice (2010), is:

$$\chi = \left(\frac{\left(\frac{a}{L}\right)^{16/3} \left(\frac{L}{H}\right)}{0.456 + \left(\frac{a}{L}\right)^{16/3} \left(\frac{L}{H}\right)} \right) \tag{5.15}$$

Note that this formulation of χ assumes only elastic deformation of the conduit, clearly a very relevant simplification given our interest in viscoelasticity. The implications for viscoelastic deformation of the conduit are discussed later in section 5.5.

This correction is applied to the linear viscoelastic model by replacing p_I with $\chi\chi_w p_{static}$ and adding the constraint shown in equation 5.11. As with the models without the fluid drag correction, we assume a value for $\left(\frac{a}{L}\right)$, exploring a range of $\left(\frac{a}{L}\right)$ to find the value that best-fit the observed lake level data. With the added fluid drag correction, the choice of $\left(\frac{a}{L}\right)$ now has a substantial effect on the model results. Appendix 5D discusses the importance of $\left(\frac{a}{L}\right)$ to greater detail. Figure 5.11 shows the approximate lake levels, drainage rates, and crack openings for the elastic and linear viscoelastic ($\eta = 1e11$ Pa · s) models for our best-fit value of $\left(\frac{a}{L}\right) = 0.51$.

The first impact of conduit size is that the value of $\left(\frac{a}{L}\right)$ has a strong impact on the timing of the lake drainage event, unlike the model without a fluid drag correction. These models predict a much longer total drainage time than Das et al. (2008) observed, as the models do not completely drain the surface lake until about 40.5 hours after the crack begins forming. However, recall that the drainage time estimated from the Greenland drainage event is based on the timing of the peak horizontal surface displacement (e.g., figure 2C of Das et al.). Thus, while our best-fit model predicts the full drainage time to be just over 40 hours, the duration of the observable lake level change fits the lake level data of Das et al. (2008) closely (figure 5.11A). The threshold for an observable change in lake level is five centimeters.

Our modeling suggests there are three phases in the lake drainage process: a long initialization period of little to no observable lake level change, a rapid acceleration in the lake drainage rate until the lake drainage is complete, and then a decelerating phase of post-drainage crack growth. The few lake level data points from the Greenland lake during the rapid drainage phase suggest that there may be an acceleration in the drainage rate until the drainage finishes. However, our models predict a longer period of acceleration and a more rapid final drainage rate than are seen observationally. The net result is that our best-fit model has observable rapid drainage for 1.8 hours, which falls into the range of potential drainage time seen by Das et al. (2008), as seen in figure 5.14.

Turning now to figure 5.11B, our drainage rates are about a factor of five larger than the rate estimated by linear interpolation between the data points of Das et al. (2008). While our modeled rate is fast, the drainage rates are within an order of magnitude of the observations, which is reasonably close considering the number of approximations going into our two-dimensional model and the sparsity of the lake level data from Das et al. (2008) during the rapid drainage phase. However, our model does predict a constant acceleration of the drainage rate up until the lake has completely drained. The observations are sparse enough to allow for either constant drainage acceleration throughout the entire drainage or a drop in the drainage rate near the end of the drainage process.

Lastly, the addition of fluid drag slightly reduces the maximum crack opening values. The smaller crack openings result in longer drainage times before the complete drainage of the surface lake. An increase in the total drainage time results in a longer basal crack. The viscoelastic models systematically predict a larger deformation than the corresponding elastic model, with the difference in peak crack opening of about 10%. However, during the post-drainage phase, the difference between the elastic and viscoelastic crack openings increases to about 15%. Such a drop in the relative crack opening in the post-drainage phase is opposite the trend seen in the models without fluid drag.

5.4.2 Surface Deformation

We now use our preferred model from figure 5.11 to estimate the expected surface motion at a point 1.7 kilometers away from the main drainage conduit—the location of the GPS station used by Das et al. (2008). We model the surface uplift using an elastic finite element model rather than the analytic estimate for uplift used by Tsai and Rice (2010), as discussed in more detail in appendix 5E. As will be shown, a basal crack can create a substantial amount of horizontal motion at the theoretical GPS location. As Tsai and Rice (2010) used the approximation that all the horizontal motion comes from the pressure within the conduit, such an analytic approximation is not valid.

Figure 5.12 shows the model results, plotted against the surface motion data of Das et al. (2008). To standardize the timing of our model results to the observations, we adopt the convention of Das et al. (2008) and assume that the surface lake finishes draining synchronously with the peak horizontal displacement. The elastic crack model is shown with dashed lines, the viscoelastic model with solid lines, and the observations with bolded lines. The blue, green, and black lines correspond to the horizontal displacement, vertical displacement, and crack opening, respectively.

Table 5.2 summarizes many of the important model and observational quantities shown in figure 5.12. The model under-predicts the value of the surface deformation at the GPS station by factors of 1.7 and 2.5 (vertical and horizontal) but predicts that the horizontal deformation should be a smaller percentage of the vertical deformation than is seen observationally. Additionally, the models suggest that the peak ground motions are contemporaneous with the peak crack opening. In the Greenland observations, there is a noticeable lag in the peak vertical motion after the peak horizontal motion. For the decay of the displacements following peak ground motion, our models do a good job fitting the relative amplitude of the vertical displacement, but predict a stronger decay of the horizontal signal than in the observations. Finally, from a qualitative perspective, our results are more peaked than the GPS observations, which have a more gradual evolution of the surface displacements.

We now consider the role that the crack length has in determining the relative horizontal and vertical displacements. Figure 5.13A shows the model results normalized by the maximum magnitude of the crack opening, thus removing any influence of the changing inlet pressure on the displacement results. The horizontal displacement has a natural high in the relative displacement amplitude, peaking when the crack is slightly longer than the distance from the conduit to the GPS location (~ 2.2 kilometers versus the GPS location at 1.7 kilometers). This behavior is unlike that of the relative vertical displacement, which grows continuously with increasing crack length. Thus, if the basal crack was allowed to grow with an infinite reservoir of water, there would be a drop in the horizontal displacement at any given point due to the geometric effect of the crack growing beneath and beyond that location. In appendix 5E, the peak horizontal displacement clearly follows the crack tip, travelling laterally away from the crack's center as the crack grows longer.

The only reason this effect is not found in our model results is because the lake drains completely before the crack lengths grows long enough to express this trend in the horizontal displacements at the GPS location. As shown in figure 5.13B, the value of the relative horizontal deformation coincidentally begins to drop around the same time that the surface lake finishes draining, masking most of this geometrically-controlled signal. However, the slight reduction in the slope near the peak of the horizontal deformation is due to the movement of the crack tip away from the GPS station.

5.5 Discussion

We are now equipped to discuss two different consequences of our supraglacial lake drainage modeling. First, our model results suggest a reinterpretation of the estimated duration of the lake drainage event from the observations of Das et al. (2008). This discussion highlights two major discrepancies between our model results and the Greenland observations: the potential deceleration of the drainage rate just before the surface lake finishes draining, and the time delay between the observed vertical and horizontal displacement peaks. Second, the general importance of viscoelasticity in correctly modeling the drainage of a supraglacial lake is addressed, with some of the remaining limitations of our model discussed.

5.5.1 Re-Evaluating Lake Drainage Timing

In Das et al. (2008), the authors estimate the total lake drainage duration based on the observed peak surface horizontal motion of their GPS station, which approximately matches a linear extrapolation of the final half-dozen lake level observations. However, as discussed in subsection 5.4.2, the peak horizontal surface displacement is controlled by the crack length in addition to the crack opening (figure 5.13). Such a relationship means that the horizontal displacement may be reflective of the crack's geometry rather than the total crack opening (and thus lake level), and that the peak value may not correspond to the end of the surface lake drainage. As the vertical surface displacements monotonically grow with crack length, we propose that using the peak vertical motion is a better estimate for the duration of the lake drainage event.

Applying this new estimate of the rapid drainage duration to the data of Das et al. (2008), the duration of the rapid lake drainage would be closer to 1.6-1.8 hours rather than the suggested 1.4 (as shown in figure 5.14). This new drainage time suggests that the lake is still draining when the monitoring station Hobo 1 is grounded. As Hobo 1 was farther away from the drainage conduit and came to rest at a higher elevation than station Hobo 2, such a result could be explained by bathymetry (i.e., after about 17:15, the lake has drained below the level of ~ 5 meters, leaving Hobo 2 stranded on the ice's surface while the lake is still draining elsewhere).

However, the two major discrepancies remain between our model results and the observations: first, our models suggest that the drainage rate accelerates until the supraglacial lake is fully drained while a constant or even reduced drainage rate is necessary to match the observed drainage duration; second, our models do not show a delay between the peak horizontal and vertical surface displacements, as is seen in the observations from Greenland.

5.5.1.1 Drainage Deceleration

Our models predict a continuous acceleration in the drainage rates until the surficial lake finishes draining, while the observations of Das et al. (2008), in conjunction with our drainage timing, do not support such a trend in drainage rate. The simplest explanation for this discrepancy is that our models are systematically missing an important process near the end of the rapid lake drainage phase that reduces the final drainage rate. As all the observational data shows, the rate of displacement slows before reaching the peak value for both the horizontal and vertical components, while our models only show this behavior in the horizontal component (and is attributable to the geometry of the crack relative to the GPS station, see section 5.4.2).

One potential process that our models miss is that the drainage conduit may act less like a drain (i.e., a completely submerged crack) and more like a moulin (i.e., water flowing into the crack from the side) as the lake level drops (shown conceptually in figure 5.15). The net result of such a transformation would be a reduction in the drainage rate late in the rapid lake drainage phase. Another possibility is that, for the observed lake drainage event, one of the two main drainage conduits stopped contributing to the lake drainage due to the falling lake level, resulting in a drop in the lake drainage rate. To test either hypothesis, a more detailed mapping of the supraglacial lake bed and/or knowing the spatial extent of the lake's surface through the drainage event would be necessary.

5.5.1.2 Displacement Peak Timing

Our models fail to reproduce the offset in the timing of the vertical and horizontal displacement peaks seen by Das et al. (2008). One potential cause is that the draining surface lake is assumed to have a constant surface area. Such an assumption is unlikely to be a good approximation for the geometry of a supraglacial lake. A change in the lake's cross-sectional area could be the cause of an apparent increased drainage rate as interpreted from the lake level data.

In our models, the net result of assuming a shrinking cross-sectional area of the lake with depth will be an increased rate of change in surface elevation due solely to bathymetry, even with a constant change in lake volume. As we fit our ideal model by changing $\left(\frac{a}{L}\right)$ until the water level of the constant-surface-area lake matched the trend in the observed lake level, having a narrowing lake would cause us to select a value of $\left(\frac{a}{L}\right)$ that is too large. Overestimating the size of the drainage conduit would lead to an elevated drainage rate and thus a shorter duration of the rapid drainage phase. Figure 5.16 shows schematically the effect of having a variable bathymetry on the observed lake level.

Having a bathymetrically variable lake does not address the need for a constant or reduced drainage rate late in the drainage process, and actually makes this issue worse, if the lake's surface area decreases as a function of depth. Needing a reduced $\left(\frac{a}{L}\right)$ to explain the surface observations would increase the crack length at complete drainage. As seen in figure 5.13, a longer crack length would cause the horizontal deformation at the GPS station to peak earlier than the vertical deformation as is seen in Das et al.'s (2008) GPS observations. However, as with the absolute drainage rates, a more detailed understanding of the bathymetry and drainage history of the supraglacial lake is necessary to test this hypothesis.

5.5.2 Influence of Viscoelasticity

A major goal of this research is to quantify the importance of using a viscoelastic rheology for ice to model the process of supraglacial lake drainage. From our modeling, viscoelasticity has three major effects on our solutions to the lake drainage problem: predicting the secession of surface drainage sooner, a larger peak crack opening, and a larger post-drainage deformation than in an equivalent elastic model.

Unfortunately, the total drainage timing is not measurable from surface observations, as the surface deformation only reaches an observable level late in the drainage process when the drainage rates rapidly accelerate. The duration of the rapid drainage phase, an easily measured time, is not strongly affected by the choice of rheology. Similarly, the peak crack opening is not currently a measurable quantity. Thus, only the relative amplitude of the post-drainage deformation provides information that can constrain the importance of viscoelasticity. However, as the difference between the viscoelastic and elastic models is expected to be about 10% for our model, this information alone is not sufficient to conclusively determine if viscoelasticity is necessary to match the observations.

Of course, the model results presented in section 5.4 are for a single linear viscosity and do not explore the full range of possible viscosities. From the definition of the consistent tangent viscoelastic compliance modulus S_{VE} (equation 5A.4), reducing the model viscosity will likewise reduce S_{VE}, resulting in increased crack opening at a given pressure. A larger crack opening increases the crack propagation speed and drainage rate, reducing the crack length at, and thus the time until, the complete drainage of the surface lake. The net result is that reducing the viscosity causes the viscoelastic solution to diverge more strongly from the elastic solution both in terms of drainage duration and deformation magnitude. The opposite is true for increasing the viscosity, which causes the solution to behave more like the elastic solution.

However, as we previously stated, the viscous deformation is demonstrably nonlinear (e.g., Glen, 1955; 1958). As shown by our constant inlet pressure PNL model (subsection 5.3.3), a nontrivial amount of viscous deformation will occur only when the effective viscosity of the nonlinear model drops substantially during the beam-like phase (when the crack length is longer than the glacier thickness). However, if the viscous crack opening becomes large, the lake will completely drain more rapidly than in the corresponding elastic model. After this point, the crack deflates, reducing the flexural stresses that control the value of the effective viscosity, resulting in a larger viscosity and a smaller proportion of viscous deformation. Thus, the nonlinear model should only vary significantly from the linear viscoelastic model during the period of rapid lake drainage, and only if the lake volume is sufficiently large to grow the basal crack longer than the glacier's thickness.

Additionally, as our cracks only grow elastically to between two and three kilometers before the surface lake finishes draining, using equation 5.10, the effective viscosity in the PNL model should not drop below about $1e11\ \mathrm{Pa \cdot s}$, suggesting that the linear results from section 5.4 represent a maximum result for any possible nonlinear viscous deformation. Thus, we must conclude that the effects of viscoelasticity on the drainage of a supraglacial lake are fairly minor (about 10% at most). While such is difference is not trivial, the effects of the conduit size on the solution are demonstrably larger (see section 5.4 and appendix 5D). We suggest that creating a physically-consistent model for the drainage conduit's evolution during the drainage process is more important to correctly model the lake drainage phenomenon than using either a linear or nonlinear viscoelastic rheology. That being said, if there is an appreciable viscoelastic effect on the growth and size of the drainage conduit, then viscoelasticity could be necessary to correctly model supraglacial lake drainage, but such modeling is beyond the scope of this project.

5.6 Summary and Conclusions

In this chapter, we presented a methodology for incorporating linear viscoelasticity into the semi-analytic model of Tsai and Rice (2010; 2012) for the growth of a subglacial crack filled with a turbulent fluid during the drainage of a supraglacial meltwater lake. From using finite element analysis to model an ice-appropriate nonlinear viscoelastic rheology, we found that we can approximate the behavior of the nonlinear model using a linear model with a time-varying effective viscosity, assuming that the inlet pressure is held constant.

Next, we applied two correction factors taken from Tsai and Rice (2010) to estimate the drainage history in our models, incorporating the effects of the finite volume of the surface lake and the reduction in inlet pressure due to drag on the fluid falling through the drainage conduit to better match the observations of a real supraglacial drainage event from Greenland (Das et al., 2008). Our modeling suggests that the estimated drainage time from Das et al. (2008) may be too short. More generally, our model results suggest that a viscoelastic rheology does not match the observations of Das et al. (2008) to a significantly greater extent than a linear elastic model does. Using our general model results for linear and nonlinear viscosity, we propose that exploring the full range of reasonable viscous parameters will not increase the divergence of the viscoelastic model from the elastic model beyond what is shown here.

Another important result of this work is that the opening of a basal crack alone is sufficient to cause horizontal as well as vertical surface deformation. This horizontal motion of a given point on the glacier's surface is dependent on the relative positions of the surface observation to the crack tip, with the horizontal displacement peaking when the crack tip is beneath the observation. Thus, unlike the vertical deformation, which necessarily increases with increasing crack opening, the horizontal deformation at a single location can peak and decay even as the crack continues to grow. This result provides a possible mechanism for explaining the observed difference in peak horizontal and vertical surface deformation seen by Das et al. (2008) during the Jakobshavn Isbrae lake drainage event.

Thus, we conclude that both using linear and nonlinear viscoelasticity has, at best, a second-order effect on the modeling of the lake drainage process. While the viscous component of deformation is not negligible (even reaching about 10% at times), our work suggests that several of the modeling assumptions have a larger impact on our model results. Such factors include the lack a physically based evolution law for the drainage conduit, not knowing the bathymetry of the draining lake, and not having a good understanding of any possible changes to the drainage process when the surface lake drains to low water levels. We suggest that the next step in better understanding and mathematically modeling the phenomenon of supraglacial lake drainage is to model the dynamic growth of the (vertical) drainage conduit, especially late in the lake drainage process.

	Variable Names	Units
A	Conduit radius	m
a_k	Fitted coefficient	--
$\boldsymbol{\mathcal{C}_{VE}}$	Consistent viscoelastic tangent matrix	Pa
c_k	Fitted coefficient	--
D	Fitted coefficient	--
E	Young's modulus	Pa
F_{21}	Force in the 21 component	N
f	Darcy-Wesibach friction factor	--
f_i	Force vector	N
f_0	Reference friction factor	--
H	Ice sheet thickness	m
Δh	FEM crack edge separation	mm
K_I	Mode 1 fracture intensity	Pa $m^{1/2}$
K_{IC}	Critical model 1 fracture intensity	Pa $m^{1/2}$
K	Nikuradse roughness height	cm
L	Crack half-length	km
n_i	Normal vector	--
p	Net fluid pressure	Pa
p_I	Inlet pressure	Pa
Re	Reynold's number	--
S_T	Traction boundary surface	--
S_U	Displacement boundary surface	--
S_{VE}	Consistent viscoelastic tangent compliance matrix	Pa^{-1}
T_i	Applied traction	Pa
t	Time	s
t_0	Current timestep	s
t_1	Next timestep	s
U	Fluid velocity	m/s
U_{2k}	Chebyshev polynomial of the second kind	--
U_{TIP}	Crack tip velocity	m/s
u	Displacement (horizontal)	m
u_i	Displacement vector	m
u_i^0	Applied displacement	m
V	Model volume	m^3
V_b	Basal crack volume	m^3
V_c	Drainage conduit volume	m^3
V_d	Volume of fluid drained	m^3
V_0	Total lake volume	m^3
w	Crack opening (deflection)	m
w_{AVE}	Average crack opening	m
w_E	Elastic crack opening	m
w_V	Viscous crack opening	m

x	Horizontal coordinate	km
α	Timestepping coefficient	--
ε	Strain	--
η	Linear viscosity	Pa s
η_{eff}	Effective viscosity	Pa s
$\tilde{\eta}_{eff}$	Equivalent effective linear viscosity	Pa s
ν	Poisson's ratio	--
ξ	Bimaterial interface coefficient	--
ρ	Fluid density	kg m^{-3}
σ	Stress	Pa
σ_{flex}	Flexural stress	Pa
σ_{ij}	Stress tensor	Pa
σ_{XZ}	Two-dimensional shear stress	Pa
τ_{max}	Maxwell relaxation time	s
ϕ	Scaled velocity	--
χ	Input pressure coefficient	--
χ_w	Fluid drag correction factor	--
^	Indicates dimensionless variable	

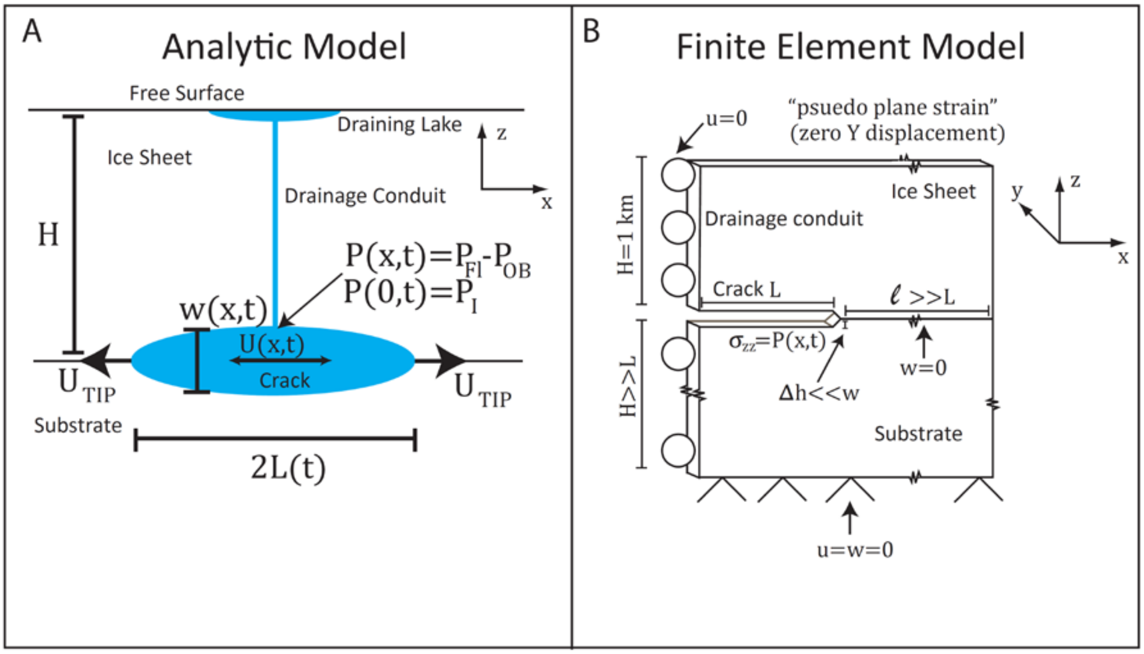

Figure 5.1: Diagrams of the lake drainage models discussed in this paper. Panel A is a schematic of the fluid-filled basal crack model used for our linear viscoelastic modeling. Panel B shows a schematic for the finite element modeling used for modeling nonlinear viscoelasticity. The details of these models are discussed in the methodology section of the main text.

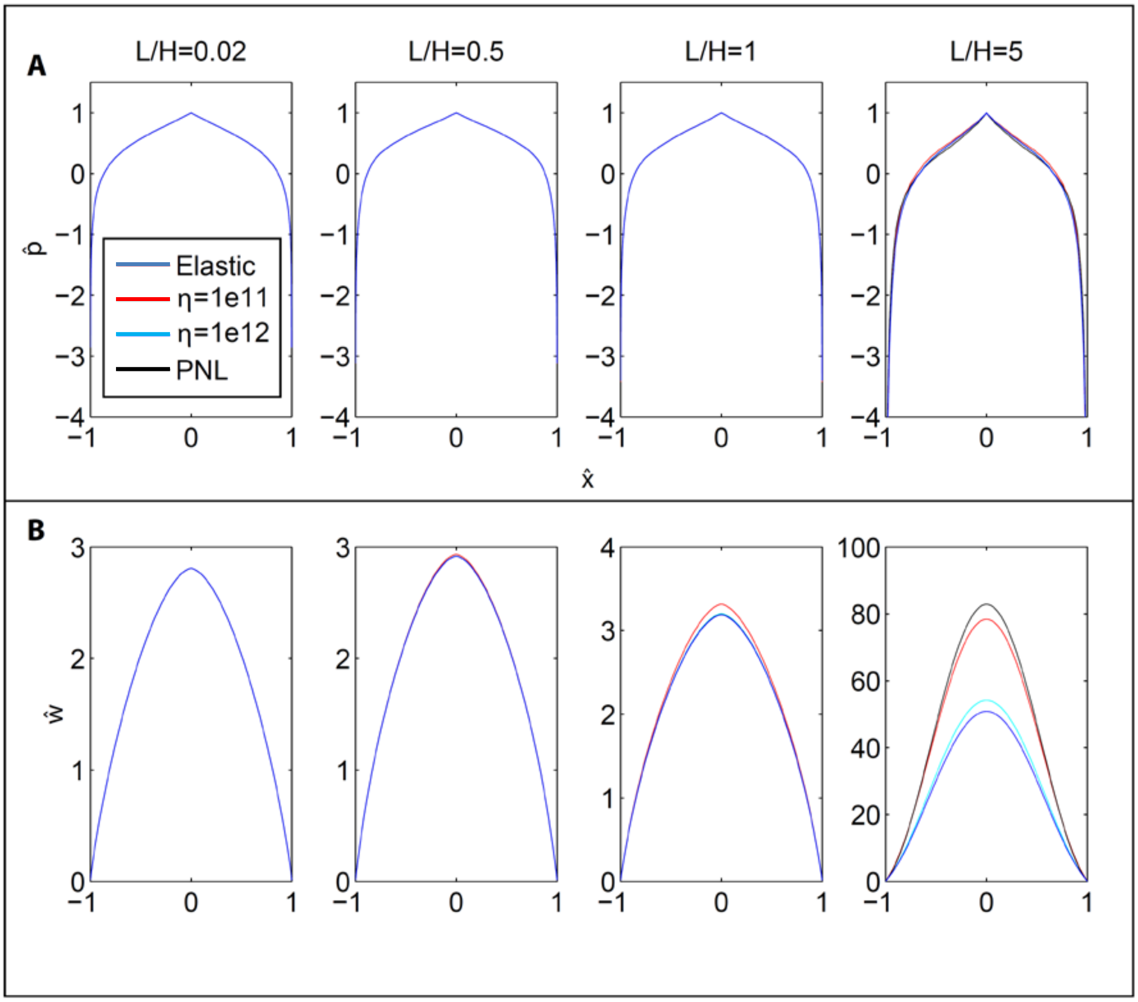

Figure 5.2: Snapshots of dimensionless pressure (panel A) and crack opening (panel B) for cracks with length *L/H=0.02, 0.5, 1*, and *5*. In all plots, there are curves representing the elastic solution, two linear viscoelastic solutions ($\eta = 10^{11}, 10^{12}$ Pa), and the pseudo-nonlinear (PNL) solution. In most of these plots, the four models have indistinguishable solutions.

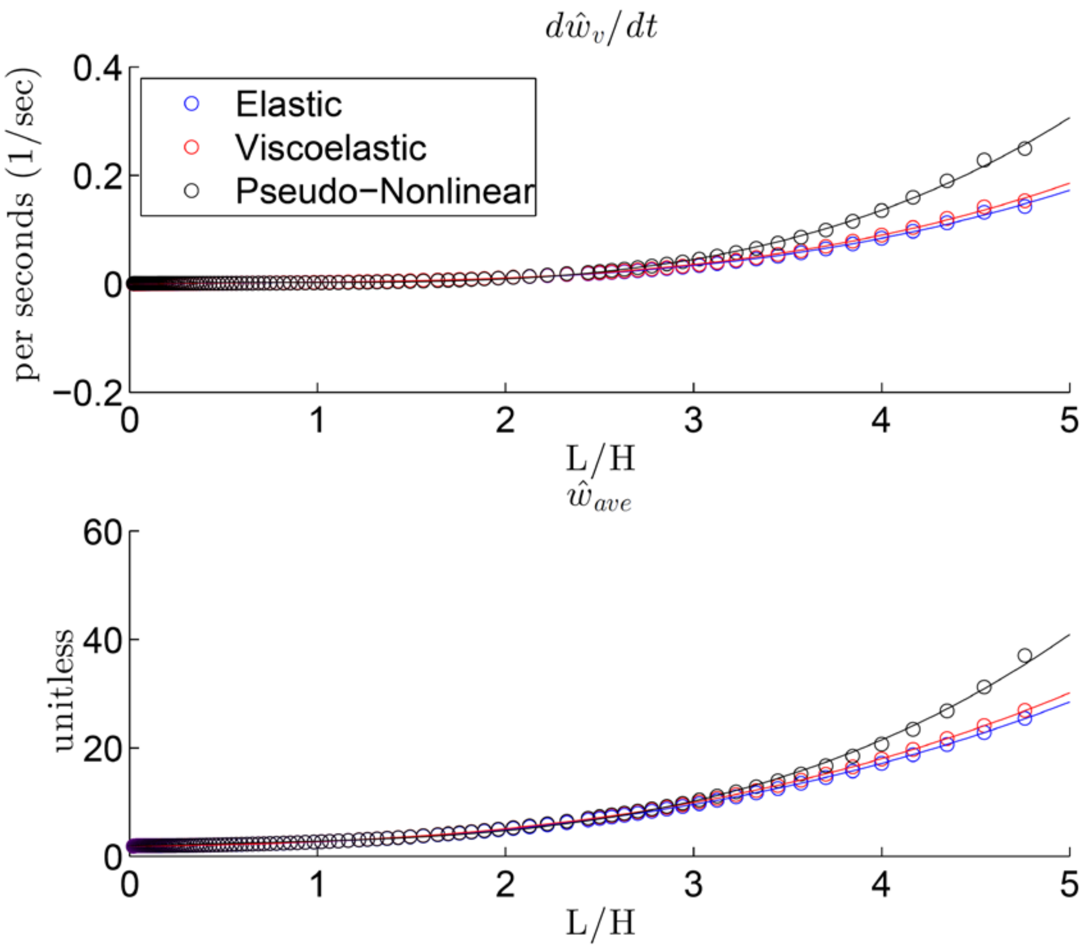

Figure 5.3: Plots showing the evolution of dimensionless crack opening as a function of crack length. The three curves plotted are the elastic solution, linear viscoelastic solution for 10^{12} *Pa*, and the pseudo-nonlinear solution. Panel A shows the rate of change of the dimensionless crack opening, while Panel B shows the value of the dimensionless crack opening. The circles represent the model output values, while the curves are polynomial fits to these data.

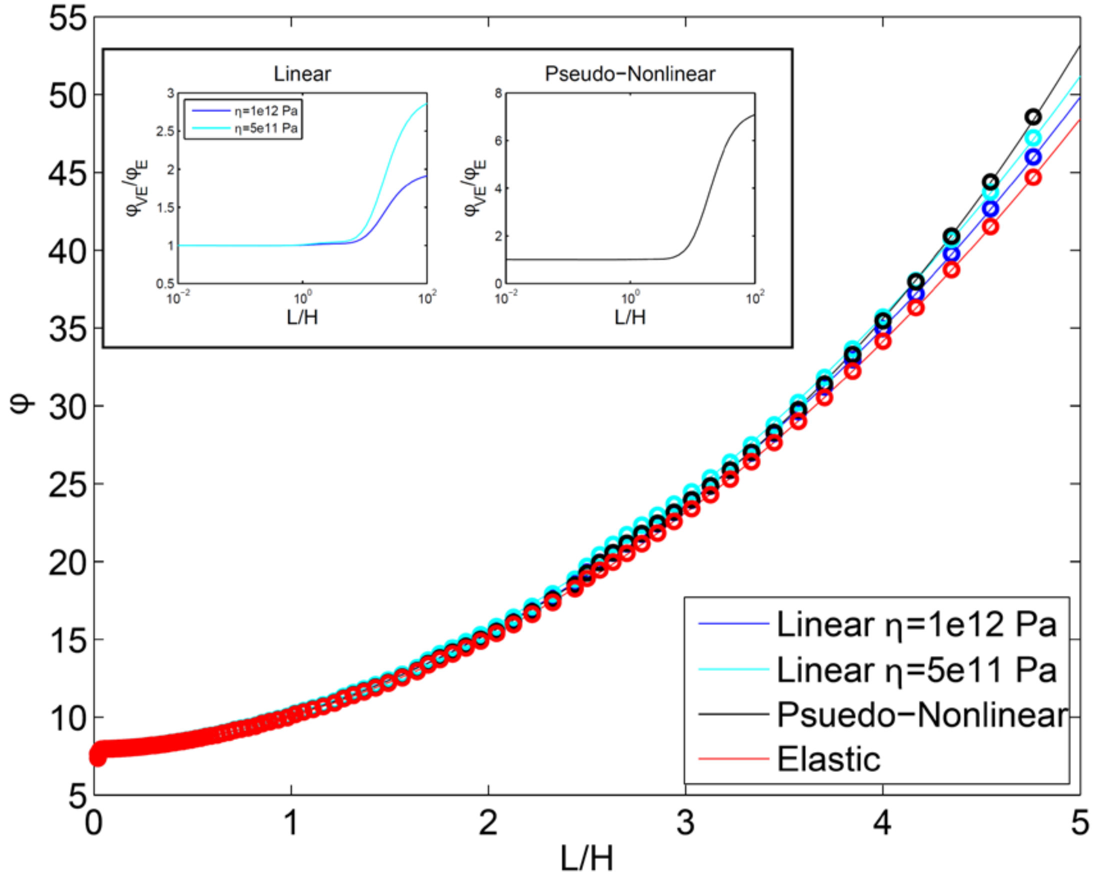

Figure 5.4: Plot of the scaled fluid velocity ϕ as a function of crack length for our elastic model, two linear viscoelastic models ($\eta = 1 \cdot 10^{11}, 5 \cdot 10^{11}$ Pa) and the pseudo-nonlinear model. The circles represent the model output values, while the curves are polynomial fits to these data. The inset figure shows the extrapolation to large and small crack lengths for the phi values of the viscoelastic models relative to the elastic model. Note that the results for the elastic model differ in magnitude from those of Tsai and Rice (2012) as we choose to neglect the bimaterial interface coefficient ξ in determining the value of ϕ, unlike Tsai and Rice (2012).

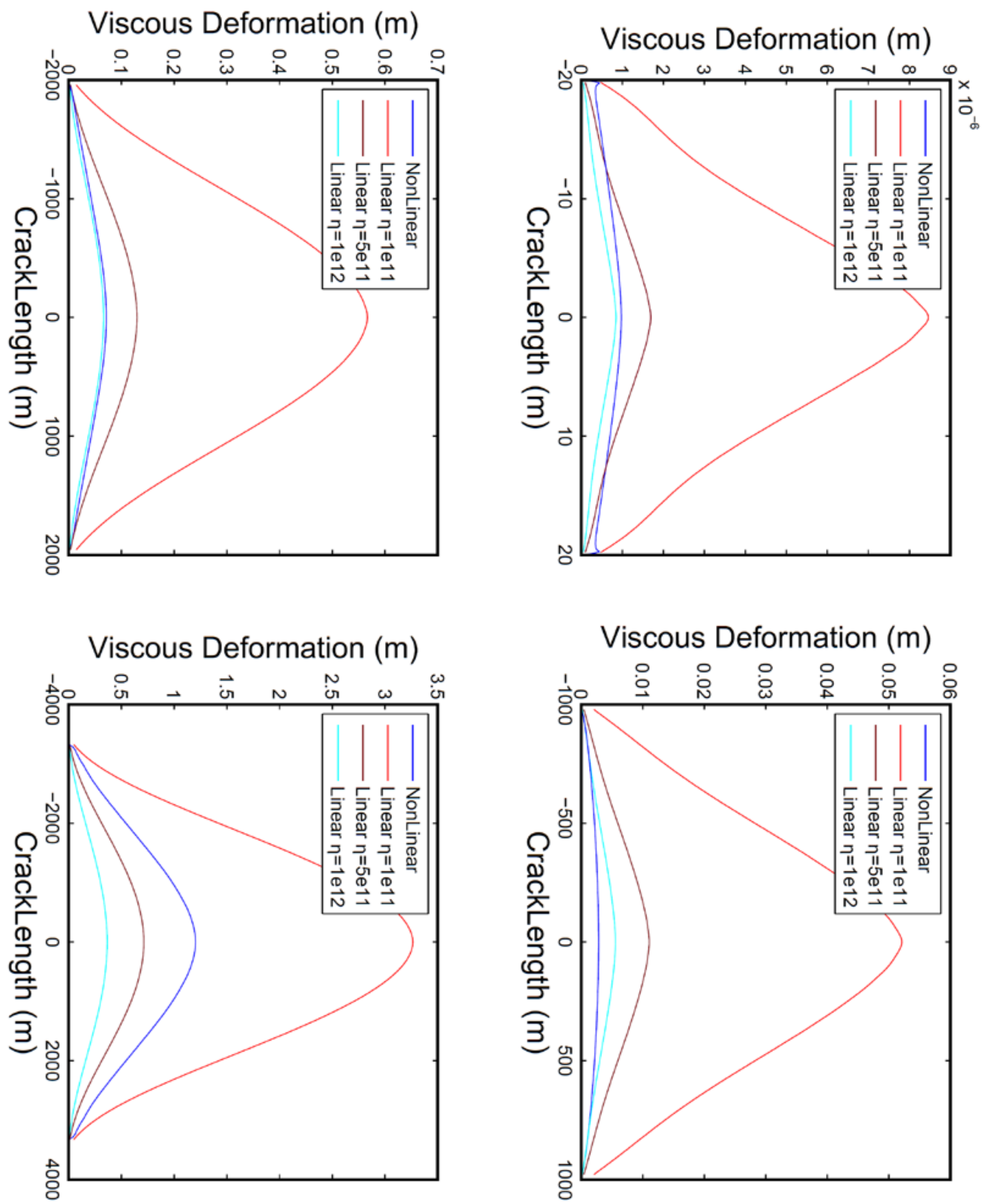

Figure 5.5: Viscous deformation at four crack lengths (20 meters, 1 kilometer, 2 kilometers, and 3.333 kilometers). The four models plotted are the nonlinear finite element model results and 3 linear viscoelastic models for a range of viscosities (1e11, 5e11, and 1e12 Pa·s).

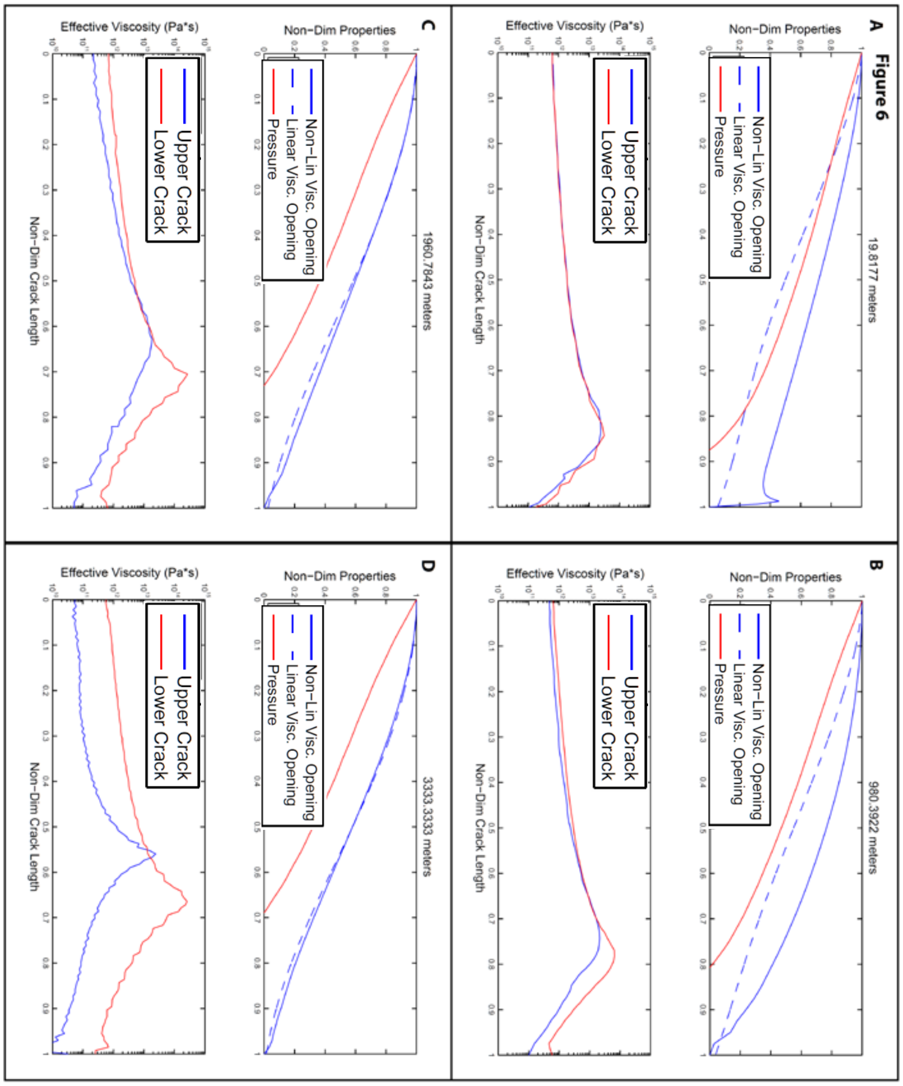

Figure 5.6: Plots showing the relationship between the normalized crack opening, normalized pressure, and effective viscosity. Panels A to D correspond to the four crack lengths shown in figure 5. In each panel, the upper plot has the normalized pressure (red) and crack opening for a linear viscoelastic (dashed blue) and nonlinear viscoelastic model (solid blue). In the lower plot, the effective viscosities for the upper (blue) and lower (red) edges of the crack are shown for the nonlinear viscoelastic model. The effective viscosity is calculated from the stress output of the finite element models.

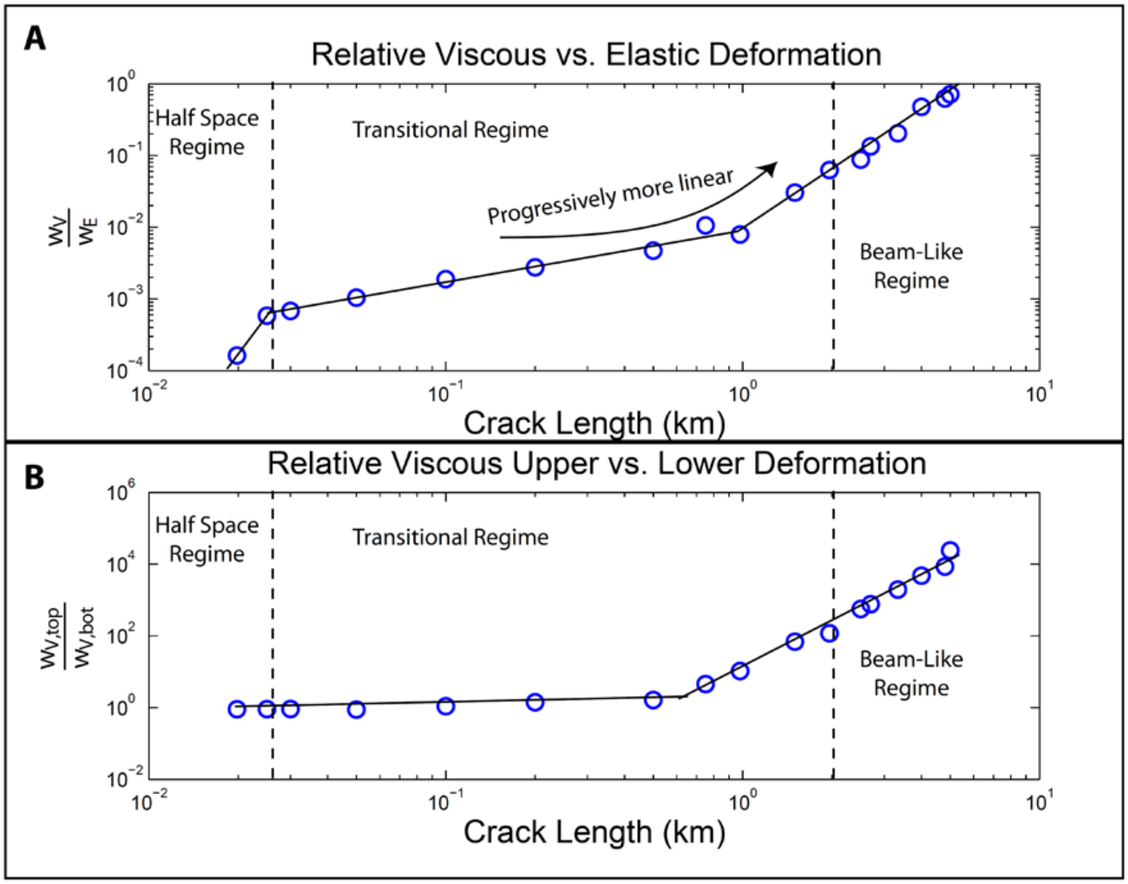

Figure 5.7: Summary figure for our nonlinear viscoelastic finite element modeling, where each point represents a separate model result. Panel A shows the relative magnitude of the viscous to elastic deformation, while Panel B shows the relative magnitude of the viscous deformation in the upper body compared to that of the lower body. The lines connecting the points are added to aid in visualizing the trend in the data. The three regimes defined in the background of each panel are defined and discussed in the main body of the text.

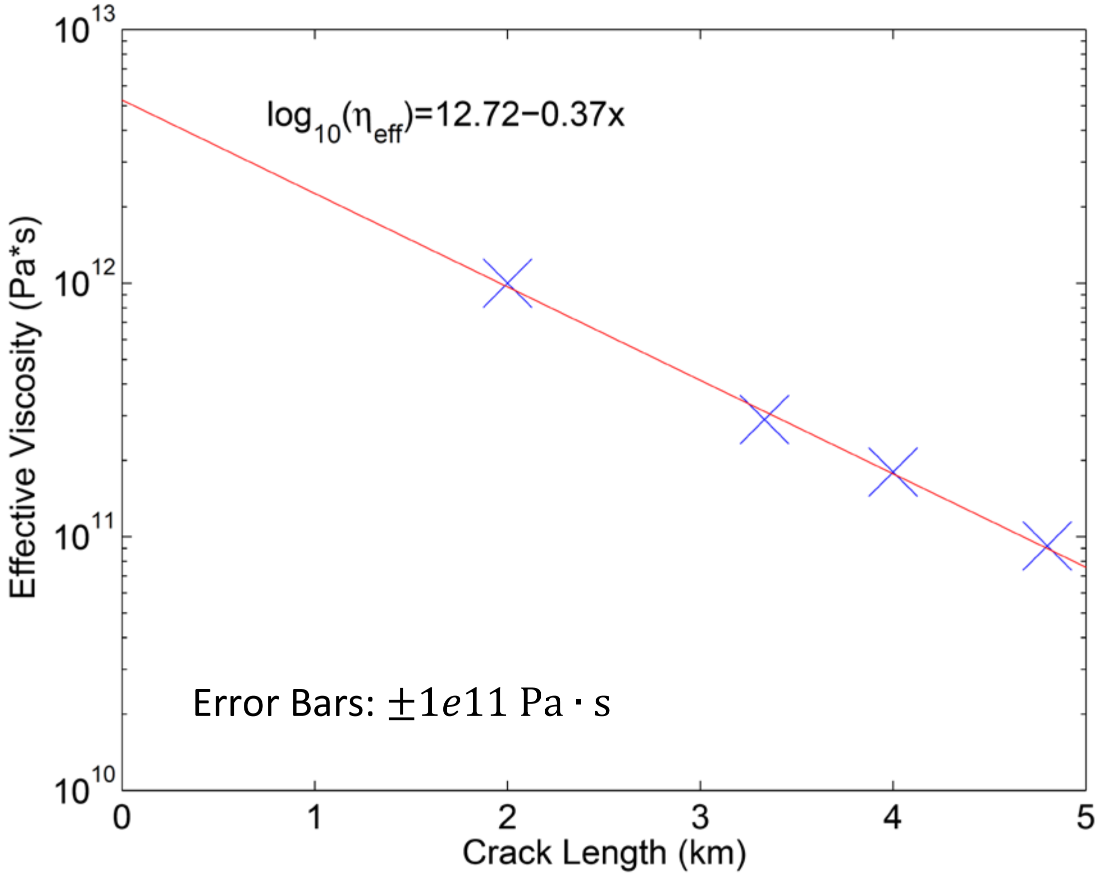

Figure 5.8: Fit of the (linear) effective viscosities approximating the nonlinear solutions as a function of crack length. See discussion in text for justification for fitting nonlinear model results with linear models. The fitted line defines the trend in effective viscosity values used to create our pseudo-nonlinear viscoelastic model.

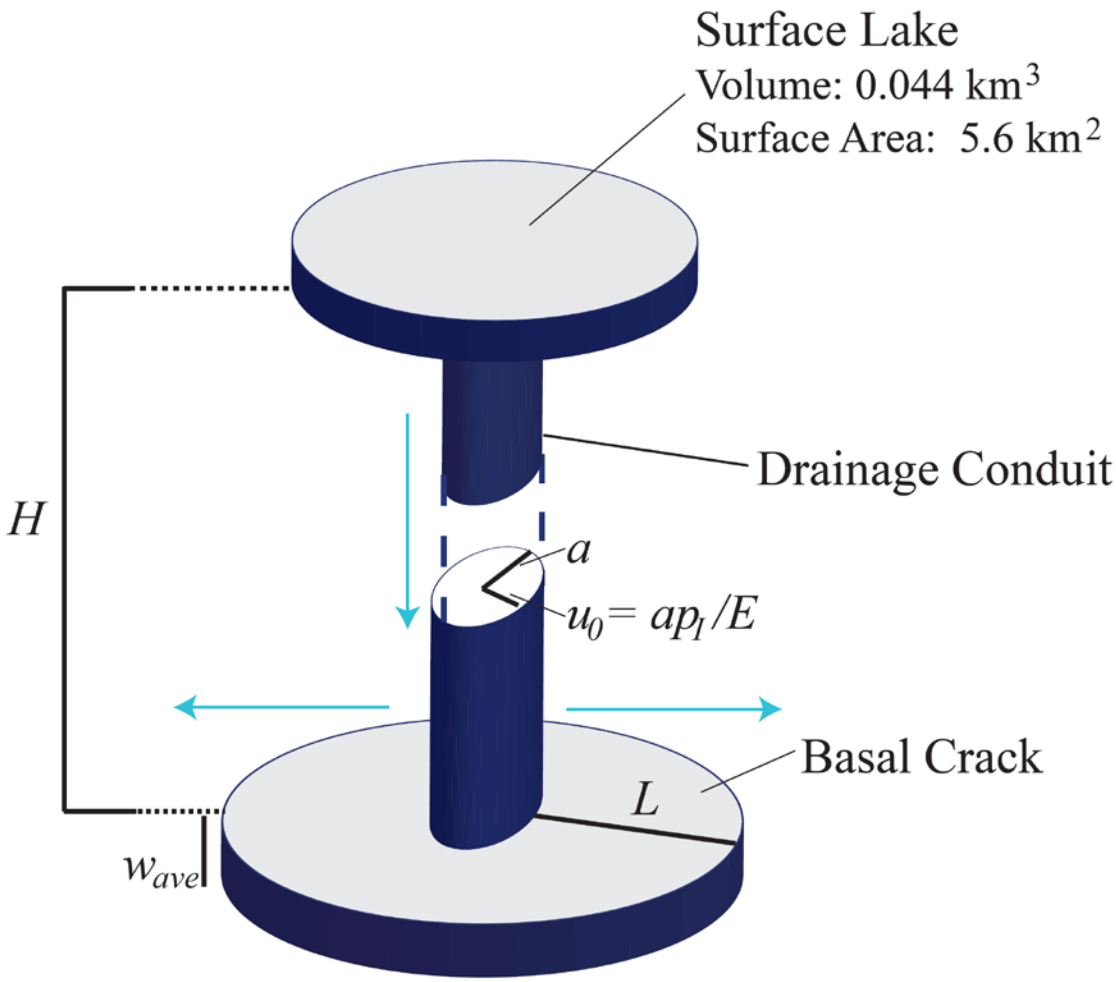

Figure 5.9: Schematic diagram of the fluid volume system used in section 5.4 to approximate the total drained fluid volume. The surface lake is assumed to have a constant surface area of 5.6 km^2, meaning that the depth is assumed to be 7.9 meter. The drainage conduit has is an ellipsoidal cylinder, with semi-major axes a and u_0. Before drainage is complete, the height of the water level in the conduit is H, the thickness of the ice. Once drainage finishes, the water level becomes H_w, as defined in equation 5.12. Finally, the basal crack is assumed to extend radially and to have a thickness of w_{ave}, the average crack opening.

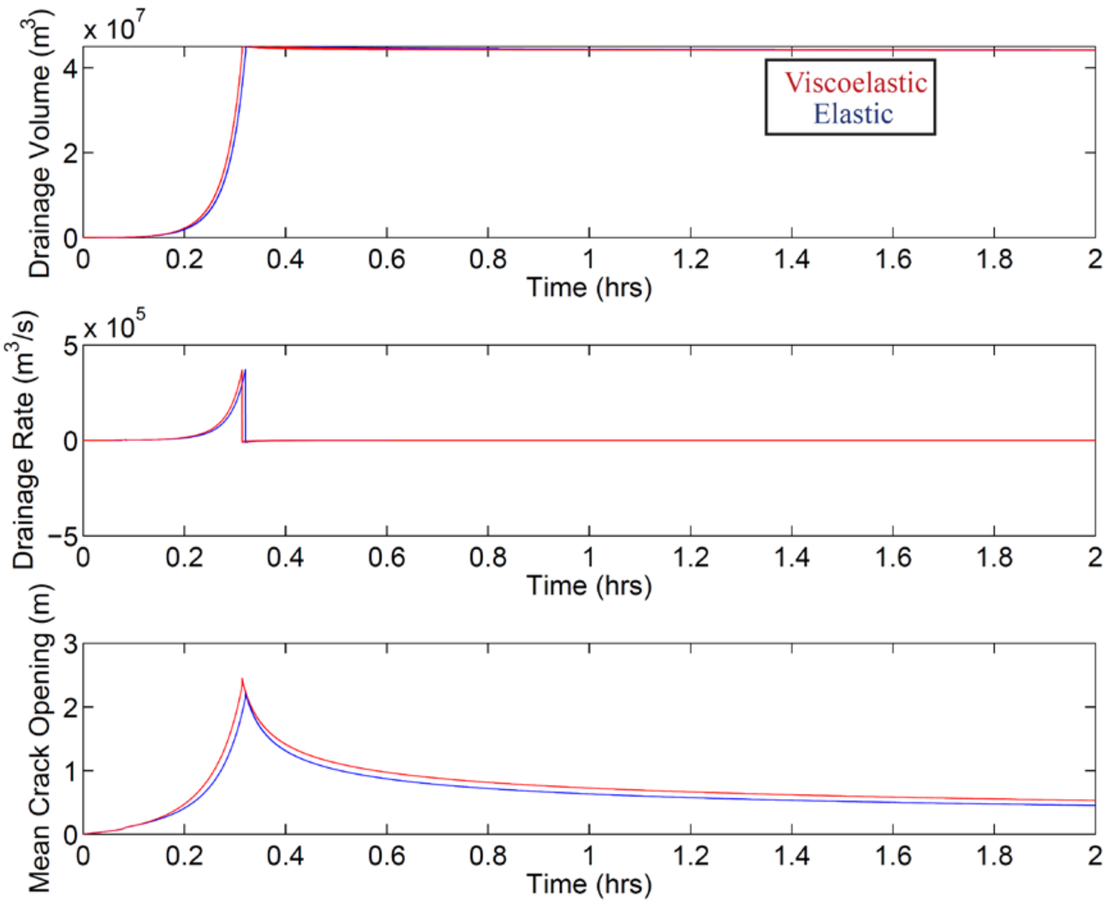

Figure 5.10: Plots of the drainage volume (A), drainage rate (B) and the average crack opening (C) for four models over a range of *a/L* values. The drainage volume and crack openings are found explicitly from our models, while the drainage rate is the time derivative of the drainage volume. The four model results are close enough to be indistinguishable from one another at the shown scale. The red lines show the results for the viscoelastic models, while the blue lines show the elastic model outputs. Note that while the models with different rheologies are not identical, the values all three parameters are similar between the two models.

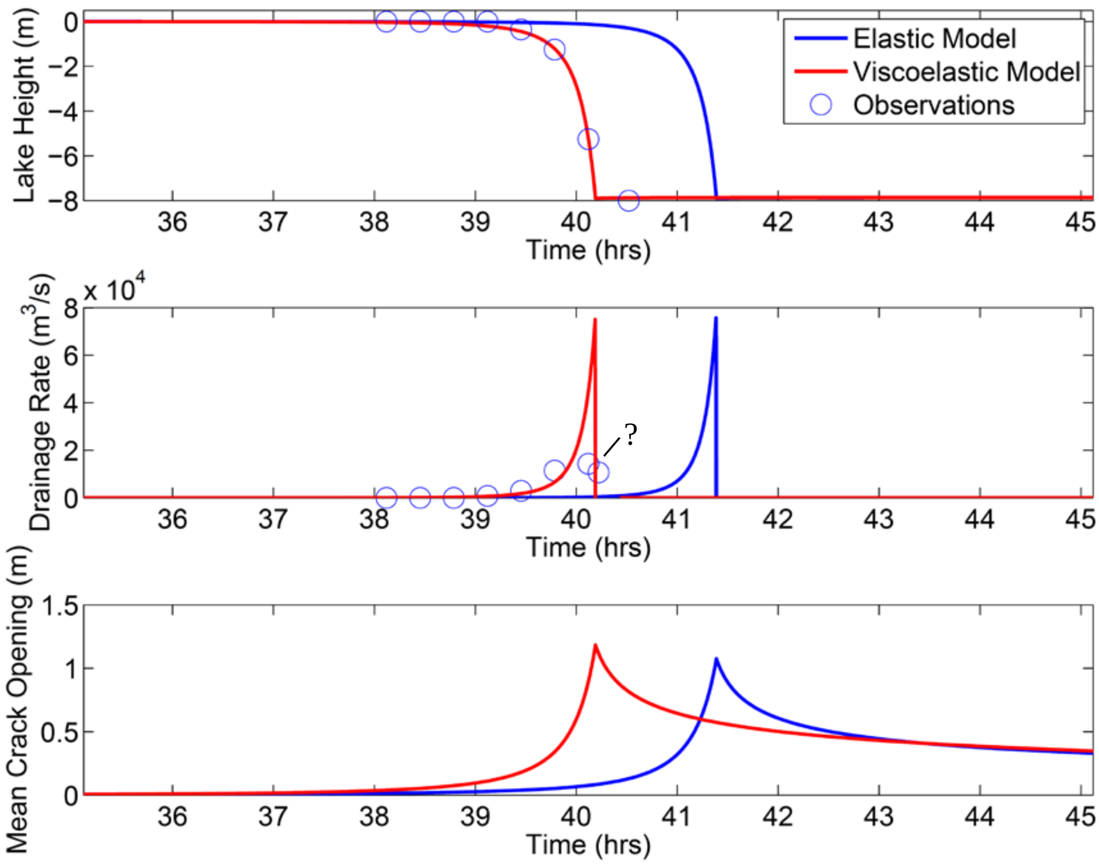

Figure 5.11: Plots of the surface lake level (A), drainage rate (B) and the average crack opening (C) for our fluid drag model with a best-fit of *a/L*=0.51. The crack openings are found explicitly from our models, while the surface lake level is calculated from the drainage volume assuming a constant lake surface area and the drainage rate is the time derivative of the drainage volume. The red lines show the results for the viscoelastic models, while the blue lines show the elastic model outputs. The circles are the lake level values taken from Das et al. (2008). The observational drainage rates are calculated from the time derivative of these values, with the peak observation drainage rate being 14,300 m^3/s. Note that the observational data have been shifted in time to overlie the model results.

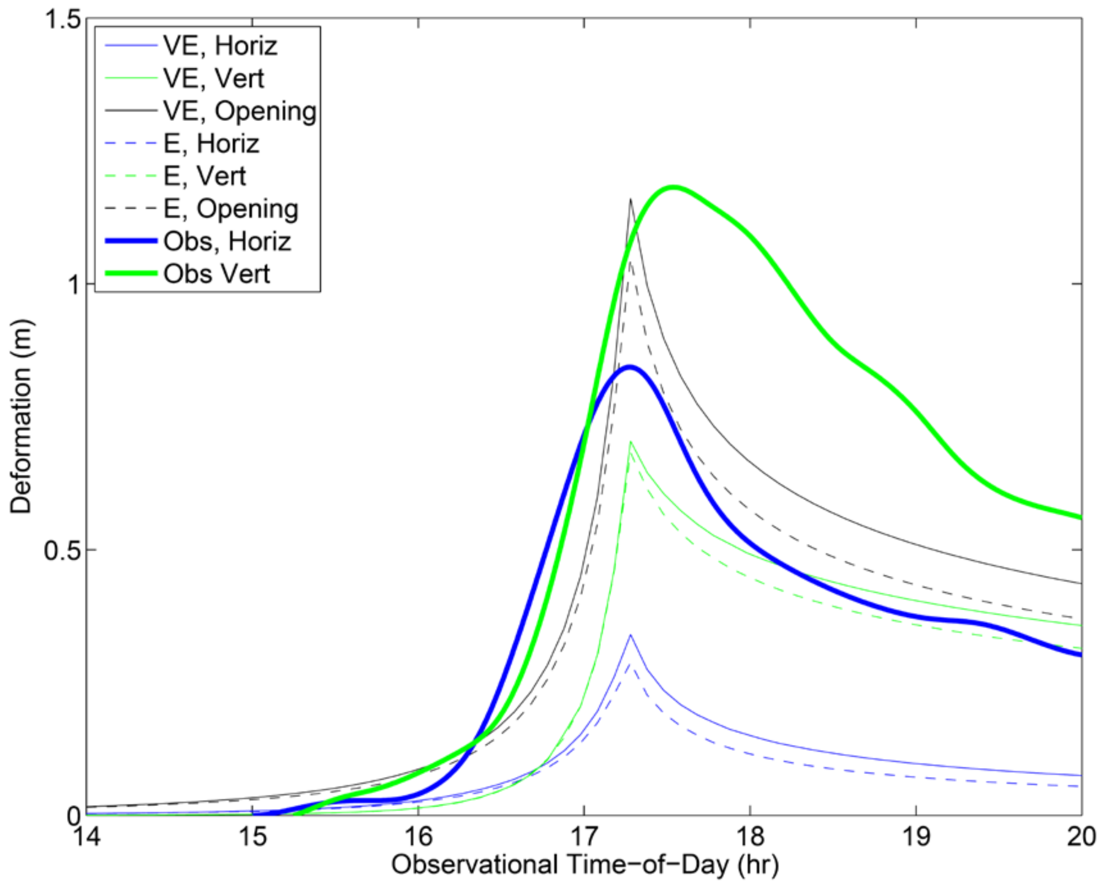

Figure 5.12: Observational and modeled surface deformation at a location 1.7 kilometers away from the main drainage conduit. Fine lines represent the viscoelastic model results, dashed lines the elastic model results, and bolded lines the observations. The line color corresponds to: blue, horizontal surface displacement; green, vertical surface displacement; black, crack opening (model only). Note that the model results are shifted in time such that the peak in horizontal deformation is the common reference time between the observations and the model results (see discussion in the main text for a justification of this reference point).

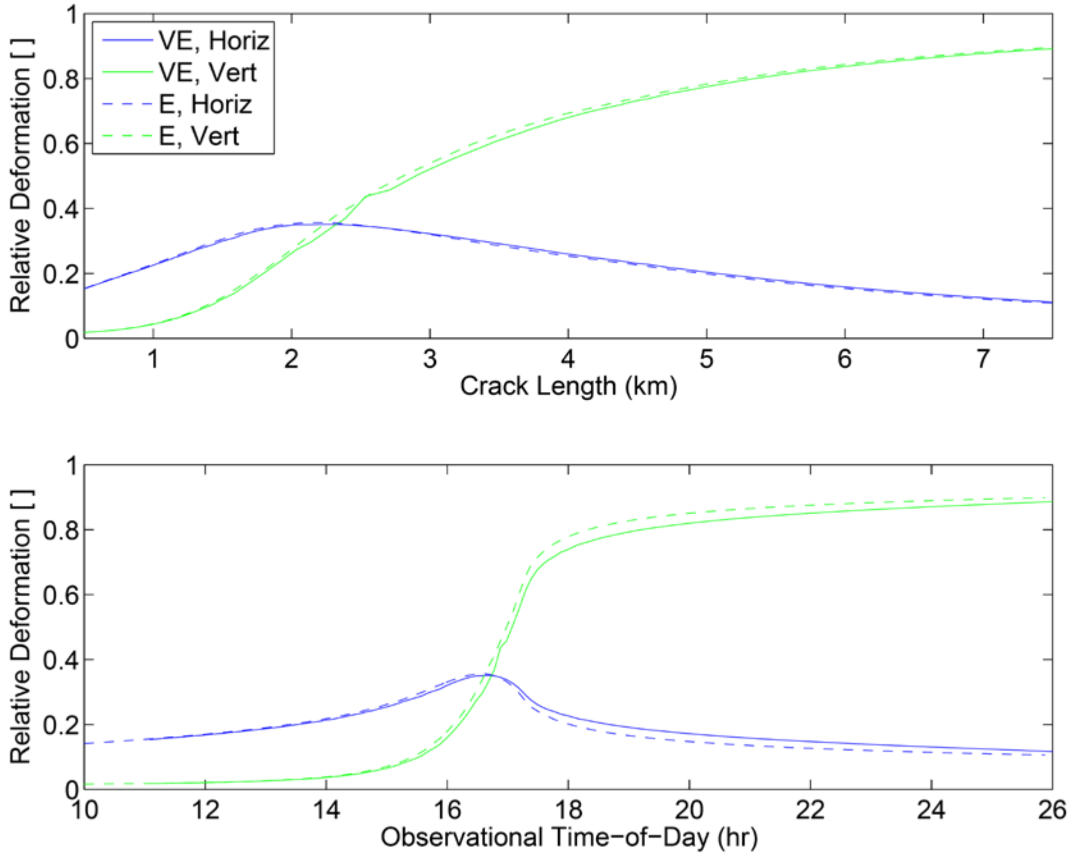

Figure 5.13: Plots of the relative surface horizontal (blue) and vertical (green) surface displacements for our elastic (dashed) and viscoelastic (solid) models, with respect to crack length (A) and time of day (B, the same horizontal scale as in figure 5.12). The relative surface displacement is the modeled surface displacement at a location 1.7 kilometers away from the main drainage conduit, divided by the maximum basal crack opening value, thus removing influence of the changing pressure from the output. The horizontal component shows a peak at about 2.2 kilometers/16.7 hours that is related only to the geometrical effect of the crack growing beneath the observational location. Such a feature is not seen in the vertical component of the relative surface deformation.

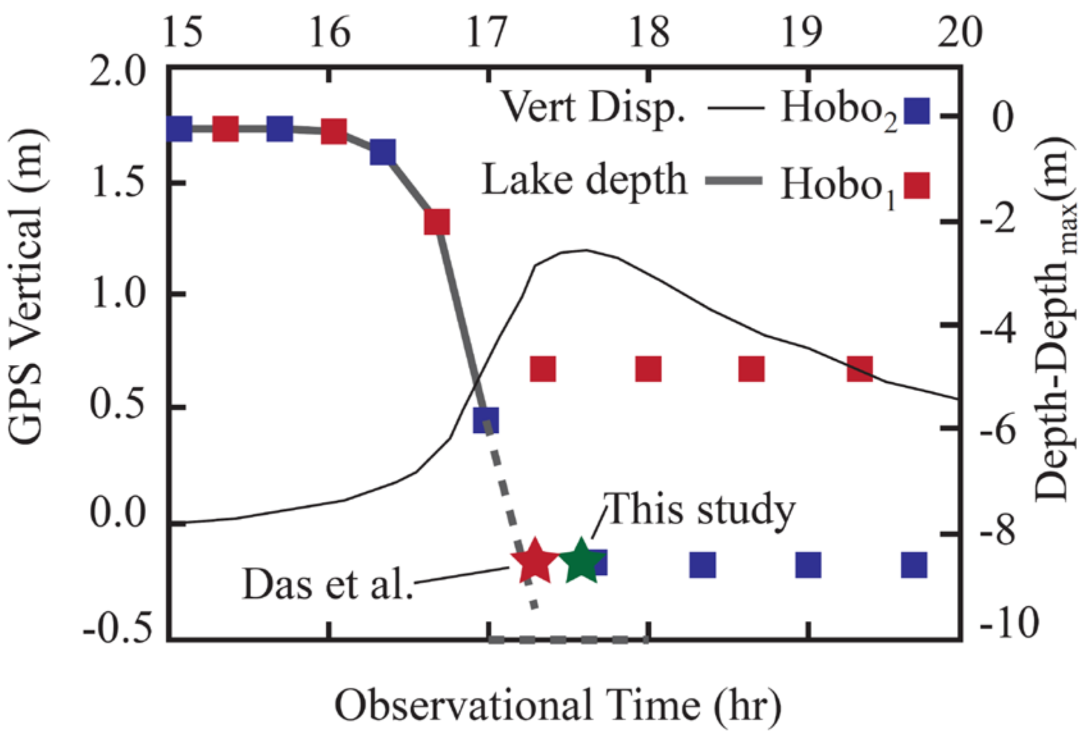

Figure 5.14: Lake level and vertical GPS data reproduced from figure 2B of Das et al. (2008). The red and blue squares are the observations of lake level from the two stations Hobo1 and Hobo2, while the thin black line is the vertical component of the GPS displacement, shifted to have a zero relative vertical offset at the start of the observational window shown in this figure. The red star shows the timing of the drainage, as estimated by Das et al. (2008), while the green star shows our estimate of the drainage timing, which is coincident with the peak in the vertical GPS displacements.

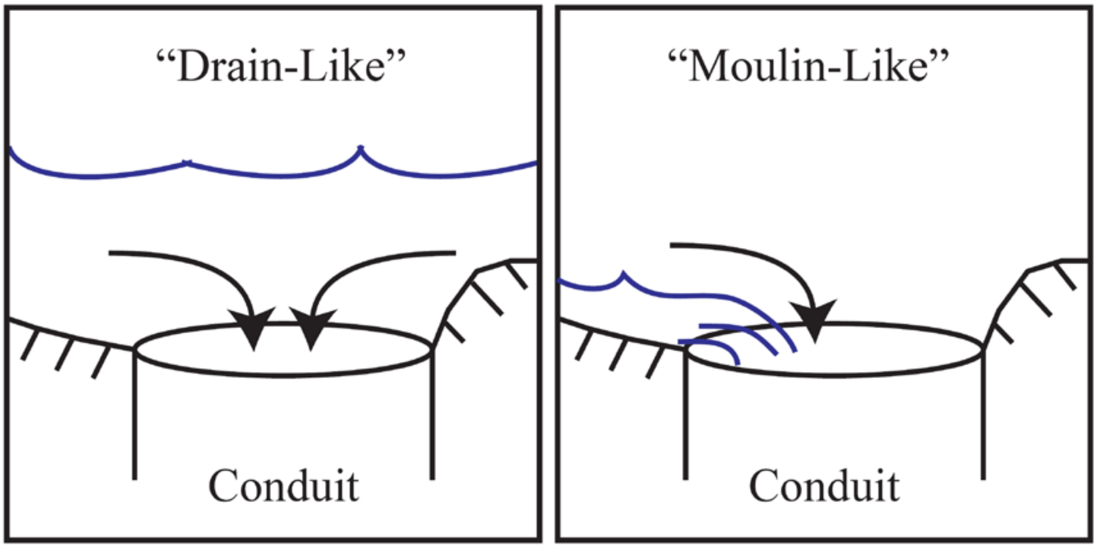

Figure 5.15: Conceptual images of the two different drainage styles described in section 5.5.1.1. The "drain-like" mode, on the left, is assumed to be the major drainage regime while the lake is at a high level. The "moulin-like" mode, on the right, is a potential style of low lake level drainage that would have a significantly reduced drainage rate, as is seen observationally when the lake is nearly completely drained.

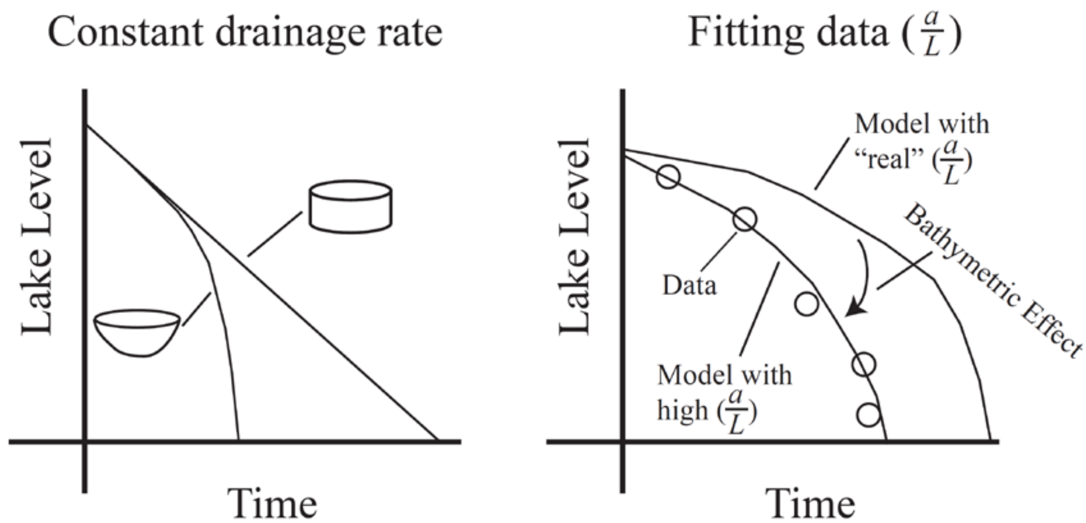

Figure 5.16: Schematic diagrams of the effects that a variable cross-sectional area of the surface lake will have on lake level observations and the problems introduced in using these data as a model constraint. The plot on the left assumes that there is a constant drainage rate of fluid into a conduit at the bottom the model lake. For a constant area lake, the lake level falls linearly; however, if the lake's area decreases with depth, the lake level fall seemingly accelerates late in the drainage process. In the plot on the right, a theoretical assemblage of lake level data is shown, with two of our model curves shown schematically. The model run with the "real" conduit size does not fit the lake level data, due to the possibility of a bathymetric effect on the lake level that is independent of the real drainage rate and conduit geometry.

Variable Name	Dimensional	Non-dimensional
Position	x	$\hat{x} = x/L$
Pressure	p	$\hat{p} = p/p_I$
Displacement	u	$\hat{u} = uE'/(p_I L)$
	w	$\hat{w} = wE'/(p_I L)$
Fluid Velocity	U	$\hat{U} = U_{tip}$
Time	t	$\hat{t} = tU_{tip}/L$
Tangent Modulus	S_{VE}	$\hat{S}_{VE} = S_{VE}/E'$

Table 5.1: List of variables with dimensional and non-dimensional versions. The constants used in the non-dimensionalization are L, crack length; p_I, input pressure; $E' = E/(1-\upsilon^2)$, the plane-strain Young's modulus; $U_{tip} = \phi U_s = \phi\sqrt{\frac{p_I}{\rho}}\left(\frac{p_I}{E'}\right)^{2/3}\left(\frac{L}{k}\right)^{1/6}$, the fluid velocity at the crack tip; ϕ, the velocity scale constant; ρ, the fluid density; and k, the Nikuradse roughness height

	Relative Peak Timing (hrs)	Peak Timing Difference (%)	Peak Magnitude (m)	Tail Magnitude at 20:00 (m)	Relative Tail to Peak (%)	Vertical to Horizontal Disp. (%)	Crack Length at Peak (km)
E, Horiz	0	0	0.29	0.055	19	234	3.661
E, Vert.	0	0	0.68	0.32	47		
VE, Horiz	0	0	0.34	0.076	22	206	3.476
VE, Vert	0	0	0.70	0.36	51		
Obs Horiz	0	0	0.84	0.30	35	140	?
Obs Vert	0.26	11.4	1.18	0.56	47		
E, Crack	0	0	1.05	0.37	35	n/a	n/a
VE, Crack	0	0	1.16	0.44	38		

Table 5.2: Quantities of interest shown in figure 5.12. E refers to the elastic models, while VE refers to the viscoelastic models. The relative peak timing is with respect to the observation and modeled horizontal displacement peak. The tail value is taken at 20:00 (20 hours), and is chosen to give a quantitative comparison of the drop in surface displacement at a time after the peak displacement. The vertical to horizontal displacement percentage is the percentage of the peak vertical displacement compared the peak horizontal displacement. Finally, the crack length at the peak is the length of the basal crack at the time of the peak displacement in that model. The crack length for the observed lake drainage event is not known. The crack rows at the bottom refer to the modeled crack opening for the elastic and viscoelastic models.

Appendix 5A: Effective Stress Formulation for Linear Viscoelasticity

Here we summarize the effective stress formulation for the deformation of a linear viscoelastic model. To begin, imagine the stress-strain relationship for a theoretical linear Maxwell viscoelastic medium, with constant moduli, under the action of a constant stress σ that is, at some time *t*, removed. From using the definition of a Maxwell material, we see immediately that the strain just before the stress is removed is:

$$\varepsilon = \frac{\sigma}{E} + \frac{t\sigma}{\eta} \tag{5A.1}$$

In equation 5A.1, the first term represents the recoverable elastic strain, while the second term is the irrecoverable viscous strain. Figure 5A.1 plots the trajectory of this relationship in stress-strain space through the entire stressing cycle. At any given time, the change in strain as a function of stress for the entire cycle up can be represented by a line connecting the origin to the current location in stress-strain space. We call the slope of this line $\boldsymbol{C_{VE}}$, the consistent viscoelastic tangent modulus. We define $\boldsymbol{C_{VE}}$ to be:

$$\boldsymbol{C_{VE}} = \frac{d\sigma}{d\varepsilon} \tag{5A.2}$$

Note that $\boldsymbol{C_{VE}}$ is dependent on the value of *t* and η, and at time $t = 0$ it is equivalent to the Young's modulus. This approach is equivalent to using the viscoelastic correspondence principle (e.g., Findley et al., 2011).

A brief summary of the derivation of $\boldsymbol{C_{VE}}$ from Aagaard et al. (2009) and Kojic and Bathe (1987) follows. Next, we define the deviatoric stress and strain tensors in the following fashion:

$$S_{ij} = \sigma_{ij} - P\delta_{ij} \tag{5A.3}$$

$$e_{ij} = \varepsilon_{ij} - \theta\delta_{ij} \tag{5A.4}$$

Where S is the deviatoric stress tensor, σ is the stress tensor, P is the hydrostatic pressure, δ is the Kronecker Delta function, e is the deviatoric strain tensor, ε is the strain tensor, and θ is the dilatation. We make the assumption that the volumetric strain is inelastic (i.e., that viscous body is incompressible), so that we can make the assertion that:

$$^{t+\Delta t}\bar{S} = \frac{^{t+\Delta t}E}{1+{}^{t+\Delta t}\nu}\left({}^{t+\Delta t}\bar{e} - {}^{t+\Delta t}\bar{e}^{P} - {}^{t+\Delta t}\bar{e}^{C}\right) \tag{5A.5}$$

$$^{t+\Delta t}\sigma_m = \frac{^{t+\Delta t}E}{1-2{}^{t+\Delta t}\nu}\left({}^{t+\Delta t}e_m - {}^{t+\Delta t}e^{th}\right) \tag{5A.6}$$

Where:

$^{t+\Delta t}\bar{S}$ is the deviatoric stress tensor defined by $^{t+\Delta t}\bar{S} = {}^{t+\Delta t}\sigma_{ij} - {}^{t+\Delta t}\sigma_m\delta_{ij}$

$^{t+\Delta t}\bar{e}$ is the deviatoric strain tensor defined by $^{t+\Delta t}\bar{e} = {}^{t+\Delta t}\varepsilon_{ij} - {}^{t+\Delta t}\varepsilon_m\delta_{ij}$

$^{t+\Delta t}\bar{e}^{P}$ is the plastic deviatoric strain tensor

$^{t+\Delta t}\bar{e}^{C}$ is the creep deviatoric strain tensor

$^{t+\Delta t}\sigma_m$ is the mean stress tensor defined by $^{t+\Delta t}\sigma_m = {}^{t+\Delta t}\sigma_{ii}/3$

$^{t+\Delta t}\varepsilon_m$ is the mean strain tensor defined by $^{t+\Delta t}\varepsilon_m = {}^{t+\Delta t}\varepsilon_{ii}/3$

$^{t+\Delta t}E$ is the Young's modulus corresponding to temperature $^{t+\Delta t}T$

$^{t+\Delta t}\nu$ is the Poisson's ratio corresponding to temperature $^{t+\Delta t}T$

$^{t+\Delta t}\varepsilon^{th}$ is the thermal strain

$t + \Delta t$ means corresponding to time $t + \Delta t$

Removing any thermal contribution from this problem and adding in the initial stress and strain states, we can rewrite (5A.5) and (5A.6) to:

$$ {}^{t+\Delta t}\bar{S} = \frac{E}{1+\nu}\left({}^{t+\Delta t}\bar{e} - {}^{t+\Delta t}\bar{e}^{P} - {}^{t+\Delta t}\bar{e}^{C} - \bar{e}^{I}\right) + \bar{S}^{I} \qquad (5A.7) $$

$$ {}^{t+\Delta t}\sigma_m = \frac{E}{1-2\nu}\left({}^{t+\Delta t}e_m - e^{I}\right) + \sigma_m^{I} \qquad (5A.8) $$

As ε_m is zero for creep and plasticity, σ_m can be found directly from equation (5A.8). Using a discrete timestep of Δt, equation (5A.7) can be rewritten as:

$$ {}^{t+\Delta t}\bar{S} = \frac{E}{1+\nu}\left({}^{t+\Delta t}\bar{e}' - \Delta\bar{e}^{P} - \Delta\bar{e}^{C}\right) + \bar{S}^{I} \qquad (5A.9) $$

Where:

$$ {}^{t+\Delta t}\bar{e}' = {}^{t+\Delta t}\bar{e} - {}^{t}\bar{e}^{P} - {}^{t}\bar{e}^{C} - \bar{e}^{I} \qquad (5A.10) $$

Thus, the problem has been reduced to determining the values of ${}^{t+\Delta t}\bar{S}$, Δe^P, and Δe^C. We now apply the implicit α-method of Bathe (1995). First, the effective creep strain is written:

$$ \boldsymbol{\Delta\bar{e}^{C}} \equiv \sqrt{\frac{2}{3}\Delta\bar{e}^{C}\cdot\Delta\bar{e}^{C}} \qquad (5A.11) $$

And the effective creep stress:

$$ \boldsymbol{{}^{t+\Delta t}\bar{\sigma}} \equiv \sqrt{\frac{3}{2}\,{}^{t+\Delta t}\bar{S}\cdot{}^{t+\Delta t}\bar{S}} \qquad (5A.12) $$

The weighted effective stress is then defined to be:

$$ \begin{aligned} {}^{\tau}\bar{\sigma} &= (1-\alpha)\,{}^{t}\bar{\sigma} + \alpha\,{}^{t+\Delta t}\bar{\sigma} \\ &= (1-\alpha)\sqrt{\frac{3}{2}\,{}^{t}\bar{S}\cdot{}^{t}\bar{S}} + \alpha\sqrt{\frac{3}{2}\,{}^{t+\Delta t}\bar{S}\cdot{}^{t+\Delta t}\bar{S}} \end{aligned} \qquad (5A.13) $$

Where α, a weighing factor, is between 0 and 1. Note that if α is equal to 0, this implicit formulation reverts to an explicit formulation. The α-method then allows us to write:

$$\boldsymbol{\Delta\bar{e}^{C}} = \Delta t\ {}^{\tau}\gamma\ {}^{\tau}\bar{S} \tag{5A.14}$$

Where:

$$^{\tau}\gamma = \frac{3}{2}\frac{\Delta\bar{e}^{C}}{\bar{\sigma}^{\tau}} \tag{5A.15}$$

$$^{\tau}\bar{S} = (1-\alpha)\ {}^{t}\bar{S} + \alpha^{t+\Delta t}\bar{S} \tag{5A.16}$$

The next step is to consider the creep rheology, which has the general form:

$$\bar{e}^{C} = f_1(\bar{\sigma})f_2(t)f_3(T) \tag{5A.17}$$

Converting the power law rheology into the effective stress formulation, we get:

$$\bar{e}^{C} = a_0(\bar{\sigma})^{a_1}(t)^{a_2}f(T) \tag{5A.18}$$

To solve this material model, first equation (5A.17) is changed into a function of incremental creep strain:

$$\boldsymbol{\Delta\bar{e}^{C}} = \Delta t f_1(\ {}^{\tau}\bar{\sigma})\dot{f}_2(\tau)f_3(\ {}^{\tau}T) \tag{5A.19}$$

where $\dot{f}_2(\tau)$is the time derivative of f_2 at weighted time τ and ${}^{\tau}T$ is the weighted temperature:

$$\tau = t + \alpha\Delta t \tag{5A.20}$$

$$^{\tau}T = (1-\alpha)\ {}^{\tau}T + \alpha^{t+\Delta t}T \tag{5A.21}$$

Now it behooves us to reformulate our creep laws into more usable forms. First, the invariants of the creep strain tensor and deviatoric stress tensors will be used in place of $\underline{e}^{C}$ and $\underline{\sigma}$, respectively. Using the example of a triaxial creep experiment with a general nonlinear viscoelastic rheology, we get:

$$\dot{e}_{11}^{C} = A_E e^{\frac{-Q}{RT}}(\sigma_1 - \sigma_3)^n = A_E e^{\frac{-Q}{RT}}\sigma_d^n \tag{5A.22}$$

In a triaxial experiment, the main stress components are $\sigma_2 = \sigma_3 = \sigma_c$which is the confining pressure of the experiment. Assuming that σ_1 is the applied stress in the main axial direction, the hydrostatic pressure can be defined to be:

$$P = \frac{\sigma_1 + 2\sigma_c}{3} \tag{5A.23}$$

And thus the deviatoric stresses are:

$$\begin{gathered} S_1 = \frac{2}{3}(\sigma_1 - \sigma_c) \\ S_2 = S_3 = -\frac{1}{3}(\sigma_1 - \sigma_c) \end{gathered} \tag{5A.24}$$

As $\sigma_c = \sigma_3$, we get:

$$\begin{gathered} S_1 = \frac{2}{3}\sigma_d \\ S_2 = S_3 = -\frac{1}{3}\sigma_d \end{gathered} \tag{5A.25}$$

Assuming the material is incompressible and isotropic, the strain rates are:

$$\begin{gathered} \dot{e}_{11}^{C} = \dot{e}_{11} \\ \dot{e}_{22}^{C} = \dot{e}_{33}^{C} = -\frac{1}{2}\dot{e}_{11} \end{gathered} \tag{5A.26}$$

Thus the second deviatoric stress and strain-rate invariants are, respectively:

$$\sqrt{J'_2} = \sqrt{-S_1S_2 - S_2S_3 - S_1S_3} = \frac{\sigma_d}{\sqrt{3}} \tag{5A.27}$$

Applying the definition 5A.27 to equation 5A.22, we get:

$$\sqrt{\dot{L}'^{C}_2} = A_E\frac{\sqrt{3}^{n+1}}{2}e^{-\frac{Q}{RT}}\sqrt{J'_2}^{n} \tag{5A.28}$$

We can compact the constants, for example:

$$A_T = A_M e^{-\frac{Q}{RT}} = A_E\frac{\sqrt{3}^{n+1}}{2}e^{-\frac{Q}{RT}} \tag{5A.29}$$

However, the formulation of A_T shown in 5A.29 is not, strictly speaking, constant as it depends of the value of the stress exponent n. This can be avoided by introducing a reference stress and strain-rate $\sigma_0$and $\dot{e}_0$such that the flow law, in terms of the second invariants, becomes:

$$\frac{\sqrt{\dot{L}'^{C}_{2}}}{\dot{e}_0} = \frac{\sqrt{J'_2}^{n}}{S_0} \tag{5A.30}$$

where

$$A_T = \frac{\dot{e}_0}{S_0^n} \tag{5A.31}$$

Thus the component form of 5A.27 can be rewritten, using 5A.29-5A.31, as:

$$\dot{e}_{ij}^{C} = \frac{\dot{e}_0 \sqrt{J'_2}^{n-1} S_{ij}}{S_0^n} \tag{5A.32}$$

Now, using equation (5A.19), we can find the incremental strain of each rheological model:

$$\begin{aligned} \boldsymbol{\Delta \bar{e}^{C}} &\approx \frac{\Delta t \dot{e}_0 \sqrt{{}^{\tau}J'_2}^{n-1} \bar{S}}{S_0^n} \\ &= \frac{\Delta t \dot{e}_0 \ {}^{\bar{\tau}}\sigma^{n-1} \bar{S}}{\sqrt{3}^{n-1} S_0^n} \end{aligned} \tag{5A.33}$$

From equation (5A.14) we can find the value of ${}^{\tau}\gamma$ and from equation (5A.15) the value of $\boldsymbol{\Delta \bar{e}^{C}}$ in the following manner:

$${}^{\tau}\gamma = \frac{\dot{e}_0 \sqrt{{}^{\tau}J'_2}^{n-1}}{S_0^n} \tag{5A.34}$$

$$\boldsymbol{\Delta \bar{e}^{C}} \approx \frac{2 \Delta t \dot{e}_0 \ {}^{\tau}\bar{\sigma}^{n}}{\sqrt{3}^{n+1} S_0^n} \tag{5A.35}$$

Plugging 5A.34, 5A.35, and 5A.16 into 5A.9 results in the following forms, assuming that the condition of ${}^{t\Delta t}\bar{e}^{P} = 0$(no plasticity) is enforced:

$${}^{t+\Delta t}\bar{S} = \frac{1}{a_E}\{\bar{e}' - \Delta t \ {}^{\tau}\gamma[(1-\alpha) \ {}^{t}\bar{S} + \alpha^{t+\Delta t}\bar{S}]\} + \bar{S}^{I} \tag{5A.36}$$

Where

$$a_E = \frac{1+\nu}{E} \tag{5A.37}$$

Equation (5A.36) can be rewritten as:

$$^{t+\Delta t}\bar{S}(a_E + \alpha\Delta t\ {}^{\tau}\gamma) = \bar{e}'' - \Delta t\ {}^{\tau}\gamma(1-\alpha)\ {}^{t}\bar{S} + \alpha^{t+\Delta t}\bar{S} + a_E\bar{S}^I \tag{5A.38}$$

Taking the scalar inner product of 5A.38 results in the form:

$$^{t+\Delta t}J'_2 a^2 - b + c\ {}^{\tau}\gamma - d^2\ {}^{\tau}\gamma^2 = F = 0 \tag{5A.39}$$

Where

$$\begin{gathered} a = a_E + \alpha\Delta t\ {}^{\tau}\gamma \\ b = \frac{1}{2}\,{}^{t+\Delta t}\bar{e}' \cdot {}^{t+\Delta t}\bar{e}' + a_E\,{}^{t+\Delta t}\bar{e}' \cdot \bar{S}^I + a_E^2 J_2'^I \\ c = \Delta t(1-\alpha)^{t+\Delta t}\bar{e}' \cdot\ {}^{t}\bar{S} + \Delta t(1-\alpha)a_E\ {}^{t}\bar{S} \cdot \bar{S}^I \\ d = \Delta t(1-\alpha)\sqrt{{}^{t}J'_2} \end{gathered} \tag{5A.40}$$

5A.39 is solved by taking the derivative of 5A.39 with respect to $\sqrt{{}^{t+\Delta t}J'_2}$. This results in a general answer, shown below as equations 5A.41 and 5A.42:

$$\frac{\delta F}{\delta\sqrt{{}^{t+\Delta t}J'_2}} = 2a^2\sqrt{{}^{t+\Delta t}J'_2} + \frac{\delta\ {}^{\tau}\gamma}{\delta\sqrt{{}^{t+\Delta t}J'_2}}(2a\alpha\Delta t^{t+\Delta t}J'_2 + c + d^2) \tag{5A.41}$$

$$\frac{\delta\ {}^{\tau}\gamma}{\delta\sqrt{{}^{t+\Delta t}J'_2}} = \frac{\dot{e}_0\alpha(n-1)\sqrt{{}^{\tau}J'_2}^{\,n-2}}{S_0^n} \tag{5A.42}$$

Lastly, we need to compute the viscoelastic tangent material matrix, which relates stress to strain. It is:

$$\boldsymbol{C_{VE}} = \frac{\delta^{t+\Delta t}\vec{\sigma}}{\delta^{t+\Delta t}\vec{\varepsilon}} \tag{5A.43}$$

The stress vector is:

$$ {}^{t+\Delta t}\vec{\sigma}_i = {}^{t+\Delta t}S_i + {}^{t+\Delta t}P_i \ \text{ for } i = 1,2,3 \qquad \text{(5A.44)} $$
$$ {}^{t+\Delta t}\vec{\sigma}_i = {}^{t+\Delta t}S_i \ \text{ for } i = 4,5,6 $$

And thus:

$$ C_{ij}^{VE} = C_{ij}^{Dev} + \frac{1}{3}\frac{E}{1-2\nu} \ \ i \le 3, j \le 3 \qquad \text{(5A.45)} $$
$$ C_{ij}^{VE} = C_{ij}^{Dev} \ \text{ otherwise} $$

To solve for C_{ij}^{Dev}:

$$ C_{ij}^{Dev} = \frac{{}^{t+\Delta t}S_i}{{}^{t+\Delta t}\varepsilon_j} = \frac{\delta^{t+\Delta t}S_i}{\delta^{t+\Delta t}e'_k}\frac{\delta^{t+\Delta t}e'_k}{\delta^{t+\Delta t}e_l}\frac{\delta^{t+\Delta t}e_l}{\delta^{t+\Delta t}\varepsilon_j} \qquad \text{(5A.46)} $$

We now solve each derivative term in 5A.46 separately, saving $\frac{\delta^{t+\Delta t}S_i}{\delta^{t+\Delta t}e'_k}$for last. By taking the derivative of equation 5A.10 with respect to ${}^{t+\Delta t}e_l$we find directly:

$$ \frac{\delta^{t+\Delta t}e'_k}{\delta^{t+\Delta t}e_l} = \delta_{kl} \qquad \text{(5A.47)} $$

And from equation 5A.4 we find:

$$ \frac{\delta^{t+\Delta t}e'_k}{\delta^{t+\Delta t}e_l} = \frac{1}{3}\begin{bmatrix} 2 & -1 & -1 \\ -1 & 2 & -1 \\ -1 & -1 & 2 \end{bmatrix} i \le l, j \le 3 \qquad \text{(5A.48)} $$
$$ = \delta_{lj} \ \text{ otherwise} $$

To solve for $\frac{\delta^{t+\Delta t}S_i}{\delta^{t+\Delta t}e'_k}$it first becomes necessary to solve several other differentiations.

First, rewrite equation 5A.38 as:

$$ F = {}^{t+\Delta t}\bar{S}(a_E + \alpha\Delta t\ {}^{\tau}\gamma) - {}^{t+\Delta t}\bar{e}'' + \Delta t\ {}^{\tau}\gamma(1-\alpha)\ {}^{t}\bar{S} - \alpha^{t+\Delta t}\bar{S} + a_E\bar{S}^I = 0 \qquad \text{(5A.49)} $$

It follows directly that:

$$ \frac{\delta F}{\delta^{t+\Delta t}e'_k} = -\delta_{ik} \qquad \text{(5A.50)} $$

And:

$$\frac{\delta F}{\delta^{t+\Delta t}S_i} = a_E + \alpha\Delta t\ {}^{\tau}\gamma + \frac{\delta\ {}^{\tau}\gamma}{\delta^{t+\Delta t}S_i}\Delta t[\alpha^{t+\Delta t}S_i + (1-\alpha)\ {}^{t}S_i] \tag{5A.51}$$

To find $\frac{\delta\ {}^{\tau}\gamma}{\delta^{t+\Delta t}S_i}$first we α-expand ${}^{\tau}\gamma$using equation 5A.34

$$ {}^{\tau}\gamma = \frac{\dot{e}_0}{S_0^n}[\alpha\sqrt{{}^{t+\Delta t}J'_2} + \sqrt{{}^{t}J'_2}]^{n-1} \tag{5A.52}$$

Now product-rule expand $\frac{\delta\ {}^{\tau}\gamma}{\delta^{t+\Delta t}S_i}$:

$$\frac{\delta\sqrt{{}^{t+\Delta t}J'_2}}{\delta^{t+\Delta t}S_i} = \frac{\delta\ {}^{\tau}\gamma}{\delta\sqrt{{}^{t+\Delta t}J'_2}}\frac{\delta\sqrt{{}^{t+\Delta t}J'_2}}{\delta^{t+\Delta t}S_i} \tag{5A.53}$$

We know one set of derivatives from equation 5A.41. The other derivative is:

$$\frac{\delta\sqrt{{}^{t+\Delta t}J'_2}}{\delta^{t+\Delta t}S_i} = \frac{{}^{t+\Delta t}W_i}{2\sqrt{{}^{t+\Delta t}J'_2}} \tag{5A.54}$$

Where

$$\begin{aligned} {}^{t+\Delta t}W_i &= {}^{t+\Delta t}S_i \ \text{ if} 1 \le i \le 3 \\ &= 2^{t+\Delta t}S_i \ \text{ otherwise} \end{aligned} \tag{5A.56}$$

Thus the solutions to $\frac{\delta\ {}^{\tau}\gamma}{\delta^{t+\Delta t}S_i}$are:

$$\frac{\delta\ {}^{\tau}\gamma}{\delta^{t+\Delta t}S_i} = \frac{\dot{e_0}\alpha(n-1)\sqrt{{}^{\tau}J'_2}^{\,n-2}\ {}^{t+\Delta t}W_i}{2\sqrt{{}^{t+\delta t}J'_2}S_0^n} \tag{5A.57}$$

Now combining 5A.51 with 5A.57 and 5A.50, and recalling the Euler chain rule shown below:

$$\frac{\delta x}{\delta y} = -\frac{\frac{\delta z}{\delta y}}{\frac{\delta z}{\delta x}} \tag{5A.58}$$

results in the following, using ${}^{\tau}S_i = \alpha^{t+\Delta t}S_i + (1-\alpha)\ {}^{t}S_i$:

$$\frac{\delta^{t+\Delta t}S_i}{\delta^{t+\Delta t}e'_k} = \frac{\delta_{ik}}{a_E + \alpha\Delta t\left[{}^{\tau}\gamma + \frac{\dot{e_0}\ {}^{\tau}S_i(n-1)\sqrt{{}^{\tau}J'_2}^{\,n-2}\ {}^{t+\Delta t}W_i}{2\sqrt{{}^{t+\delta t}J'_2 S_0^n}}\right]} \tag{5A.59}$$

Now C_{ij}^{VE} can be solved for:

$$C_{ij}^{VE} = \frac{1}{3}\frac{E}{1-e\nu}\begin{bmatrix}1&1&1&0&0&0\\1&1&1&0&0&0\\1&1&1&0&0&0\\0&0&0&0&0&0\\0&0&0&0&0&0\\0&0&0&0&0&0\end{bmatrix} + \frac{1}{3}\frac{\delta^{t+\Delta t}S_i}{\delta^{t+\Delta t}e'_k}\begin{bmatrix}2&-1&-1&0&0&0\\-1&2&-1&0&0&0\\-1&-1&2&0&0&0\\0&0&0&3&0&0\\0&0&0&0&3&0\\0&0&0&0&0&3\end{bmatrix} \tag{5A.60}$$

Modifying equation 5A.60 to represent a plane-strain condition for two-dimensions, we find that the consistent viscoelastic tangent modulus is:

$$\boldsymbol{C_{VE}} = \frac{1}{3}\left(\frac{E}{1-2\nu}\right)\begin{bmatrix}1&1&0\\1&1&0\\0&0&1\end{bmatrix} + \frac{1}{3}\left(\frac{1+\nu}{E}+\frac{\alpha\Delta t}{2\eta}\right)^{-1}\begin{bmatrix}2&-1&0\\-1&2&0\\0&0&3\end{bmatrix} \tag{5A.61}$$

This definition of $\boldsymbol{C_{VE}}$ relies on the definition of the parameter α, which comes from the alpha-method of time discretization (Bathe, 1995). For our purposes, α will always be set to 1; this ensures that we are advancing the time step implicitly (such an α value is consistent with the timestepping presented in equation 9).

To match the rheological formulation shown in equation 5.4, we then convert $\boldsymbol{C_{VE}}$ into the consistent viscoelastic tangent compliance modulus S_{VE} by taking the inverse of $\boldsymbol{C_{VE}}$. Thus we get:

$$S_{VE} = \begin{bmatrix} \dfrac{\left(\frac{\alpha\Delta t}{2\eta} + 3\left(\frac{1-\nu}{E}\right)\right)\left(\frac{\alpha\Delta t}{2\eta} + \frac{1+\nu}{E}\right)}{\frac{\alpha\Delta t}{\eta} + \frac{3}{E}} & -\dfrac{\left(\frac{3\nu}{E} + \frac{\alpha\Delta t}{2\eta}\right)\left(\frac{\alpha\Delta t}{2\eta} + \frac{1+\nu}{E}\right)}{\frac{\alpha\Delta t}{\eta} + \frac{3}{E}} & 0 \\ -\dfrac{\left(\frac{3\nu}{E} + \frac{\alpha\Delta t}{2\eta}\right)\left(\frac{\alpha\Delta t}{2\eta} + \frac{1+\nu}{E}\right)}{\frac{\alpha\Delta t}{\eta} + \frac{3}{E}} & \dfrac{\left(\frac{\alpha\Delta t}{2\eta} + 3\left(\frac{1-\nu}{E}\right)\right)\left(\frac{\alpha\Delta t}{2\eta} + \frac{1+\nu}{E}\right)}{\frac{\alpha\Delta t}{\eta} + \frac{3}{E}} & 0 \\ 0 & 0 & \dfrac{1+\nu}{E} + \dfrac{\alpha\Delta t}{2\eta} \end{bmatrix} \tag{5A.62}$$

For cases where the viscous deformation is negligible, S_{VE} simplifies to the standard elastic compliance matrix in two-dimensions.

	Variable Names (Appendix 5A)	Units
A_E	Viscosity coefficient	$Pa^{-n}\ s^{-1}$
A_M	Triaxial viscosity coefficient	$Pa^{-n}\ s^{-1}$
A_T	Temperature-variable triaxial viscosity coefficient	$Pa^{-n}\ s^{-1}$
a	Placeholder variable, see 5A.40	Pa^{-1}
a_E	Placeholder variable, see 5A.37	Pa^{-1}
b	Placeholder variable, see 5A.40	--
$\boldsymbol{C_{VE}}$	Consistent viscoelastic tangent matrix	Pa
C^{Dev}	Deviatoric consistent viscoelastic tangent matrix	Pa
c	Placeholder variable, see 5A.40	Pa s
d	Placeholder variable, see 5A.40	$Pa^2\ s^2$
e_{ij}	Deviatoric strain tensor (component form)	--
$\bar{e}$	Deviatoric strain tensor	--
$\bar{e}'$	Deviatoric strain (elastic)	--
$\bar{e}^C$	Deviatoric creep strain	--
$\bar{e}^P$	Deviatoric plastic strain	--
F	Inner product of 5A.38	--
J_2'	Second deviatoric stress invariant	Pa
$\dot{L}'^C_2$	Second deviatoric strain-rate invariant	s^{-1}
n	Power law exponent	--
P	Hydrostatic pressure	Pa
Q	Activation energy	J
R	Universal gas constant	$J\ mol^{-1}\ K^{-1}$
$\bar{S}$	Deviatoric stress tensor	Pa
S_{ij}	Deviatoric stress tensor (component form)	Pa
S_{VE}	Consistent viscoelastic compliance tangent matrix	Pa^{-1}
T	Temperature	°C
t	Current time	s
W_i	Placeholder variable, see 5A.56	Pa
α	Time-weighing factor	--
γ	Creep strain increment	$Pa^{-1}\ s^{-1}$
Δt	Timestep	s
$\Delta\bar{e}^C$	Discrete deviatoric creep strain increment	--
$\boldsymbol{\Delta\bar{e}^C}$	Effective creep strain	--
$\Delta\bar{e}^P$	Discrete deviatoric plastic strain increment	--
δ	Kronecker delta function	--
$\dot{\varepsilon}_0$	Reference strain rate (material)	s^{-1}

ε_{ij}	Strain tensor (component form)	--
ε_m	Mean strain tensor	--
ε^{th}	Thermal strain tensor	--
η	Linear viscosity	Pa s
θ	Dilatation	--
$\bar{\boldsymbol{\sigma}}$	Effective creep stress	--
σ_c	Triaxial confining stress	Pa
σ_d	Triaxial deviatoric stress	Pa
σ_{ij}	Stress tensor (component form)	Pa
σ_m	Mean stress tensor	Pa
"$\dot{\ }$"	Indicates time derivative	
"^{I}"	Indicates initial condition	
"^{t}"	Indicates current timestep	
"$^{t+\Delta t}$"	Indicates next timestep	
"$^{\tau}$"	Indicates time-weighted version	

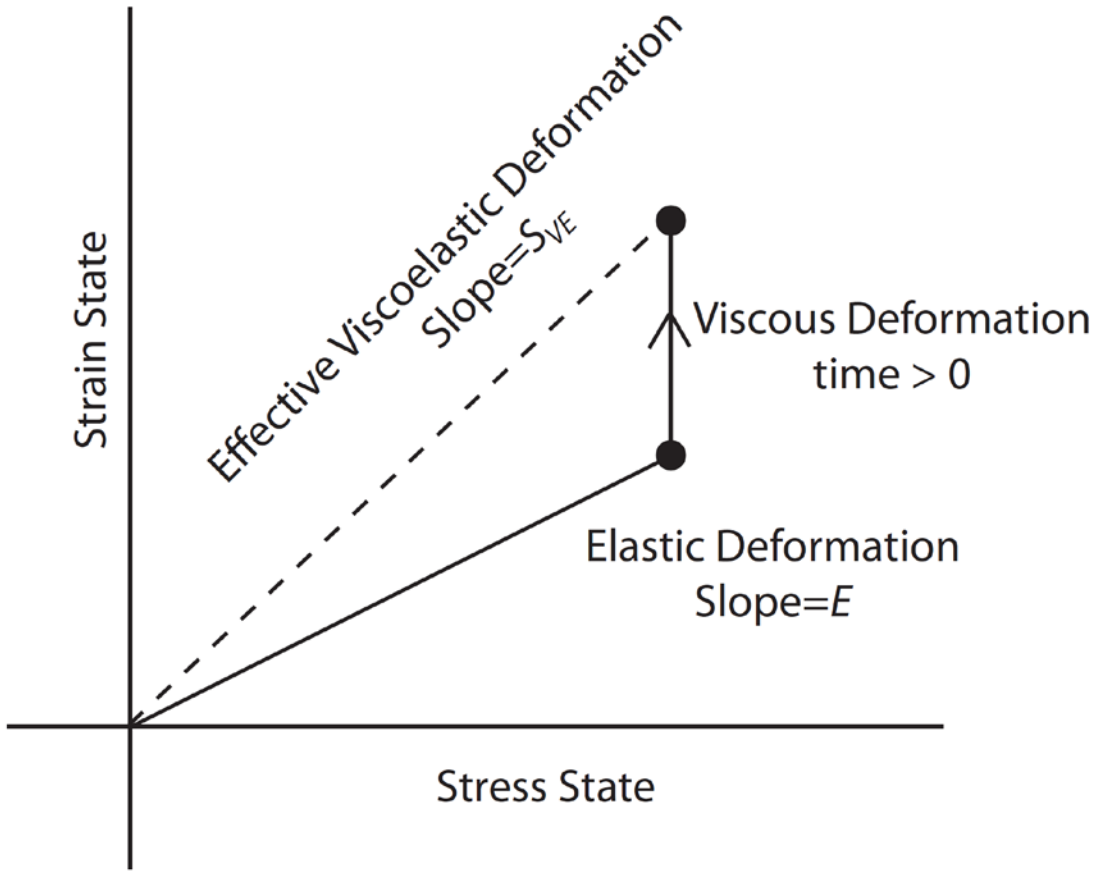

Figure 5A.1: Schematic view demonstrating the effective stress formulation. For a given (constant) stress state, the strain state moves instantaneously to an elastic configuration. Over time, the material evolves viscously to a new strain state. The slope to this a given point along the viscous deformation path is the consistent tangent modulus discussed in Appendix A.

Appendix 5B: Expected Deformation of a 1D Inhomogeneous Bernoulli-Euler Beam

To gain an understanding of the result of a stress-dependent viscosity within the beam-like deformation regime, we model a one-dimensional Bernoulli-Euler beam with a raised Young's modulus near the center of the beam. We are justified in using the linear elastic solution to infer the behavior of the nonlinear viscoelastic solution as: 1) the nonlinear case converges to the linear solution in the beam-like regime; 2) a linear elastic solution can be connected to the appropriate linear viscoelastic solution through the correspondence principle (e.g., Findley at al., 2011).

The governing equation for a Bernoulli-Euler beam with inhomogeneous elasticity under the action of a distributed pressure is:

$$\frac{\partial^2}{\partial x^2}\left(E(x)I\frac{\partial^2 w}{\partial x^2}\right) = p(x) \tag{5B.1}$$

We impose a fixed ($w = \frac{\partial w}{\partial x} = 0$) condition on one end of the beam, and impost a sliding ($\frac{\partial w}{\partial x} = \frac{\partial^3 w}{\partial x^3} = 0$) condition on the other side.

We begin by applying a constant pressure distribution to the series of elastic models summarized in table 5B.1, exploring the impact of the following three moduli profiles: 1) changes in the magnitude of the "peaked" modulus in the center of the beam; 2) changes in the width of the this modulus peak; 3) changes in the modulus at the edge of the beam. Figure 5B1.A shows the results for these models with a constant pressure, with the upper panel showing absolute deflection w, and the lower pattern showing the normalized value of deflection w/w_{max}. We see that while many of the models with raised central Young's modulus have reduced absolute deflection compared to the homogenous model, the value of the moduli at the ends of the beam have a much stronger impact on the overall deflection value. To quantify the "closeness" of the two normalized profiles, we plot the R^2 value of the normalized models compared to the linear model in figure B2. The red circles correspond to the constant edges, while the blue circles correspond to models with linearly varying moduli in the edge of the beam. We see clearly that the variation from the homogeneous model is larger with edge variable elasticity, though we note that all the values fall beneath an R^2 of 0.994, suggesting that the all models are very close to a linear solution with an appropriately chosen effective Young's modulus.

Of course, our pressure distribution is not constant in our problem, but changes along the crack profile. To investigate the impact of a variable pressure distribution on the beam model results, we now run the same 18 models with a pressure distribution that varies linearly from $-p_I$ to $+p_I$ over the length of the beam. These model results are shown in figure B1B and the R2 values are shown as X's in figure B2. We see immediately that the models with the variable pressure profile are closer to linear than those with the constant pressure distribution.

Thus, we can use these linear elastic model results to approximate the expected linear viscoelastic response by replacing the Young's modulus with the linear viscosity profile multiplied by the time over which the pressure is applied ($E(x) \to \eta(x)\Delta t$). As a nonlinear viscoelastic model is equivalent to a linear model with a stress-dependent effective viscosity (e.g., see appendix 5A), we can use these one-dimensional models to predict the impact of having a centralized region of increased effective viscosity, as is seen in the beam-like regime for our nonlinear viscoelastic models. While we never expect the nonlinear solution to converge to the linear solution as long as there is a variation in the effective modulus, these results demonstrate that we can approximate our nonlinear model with a linear model with varying viscosity with a high degree of certainty.

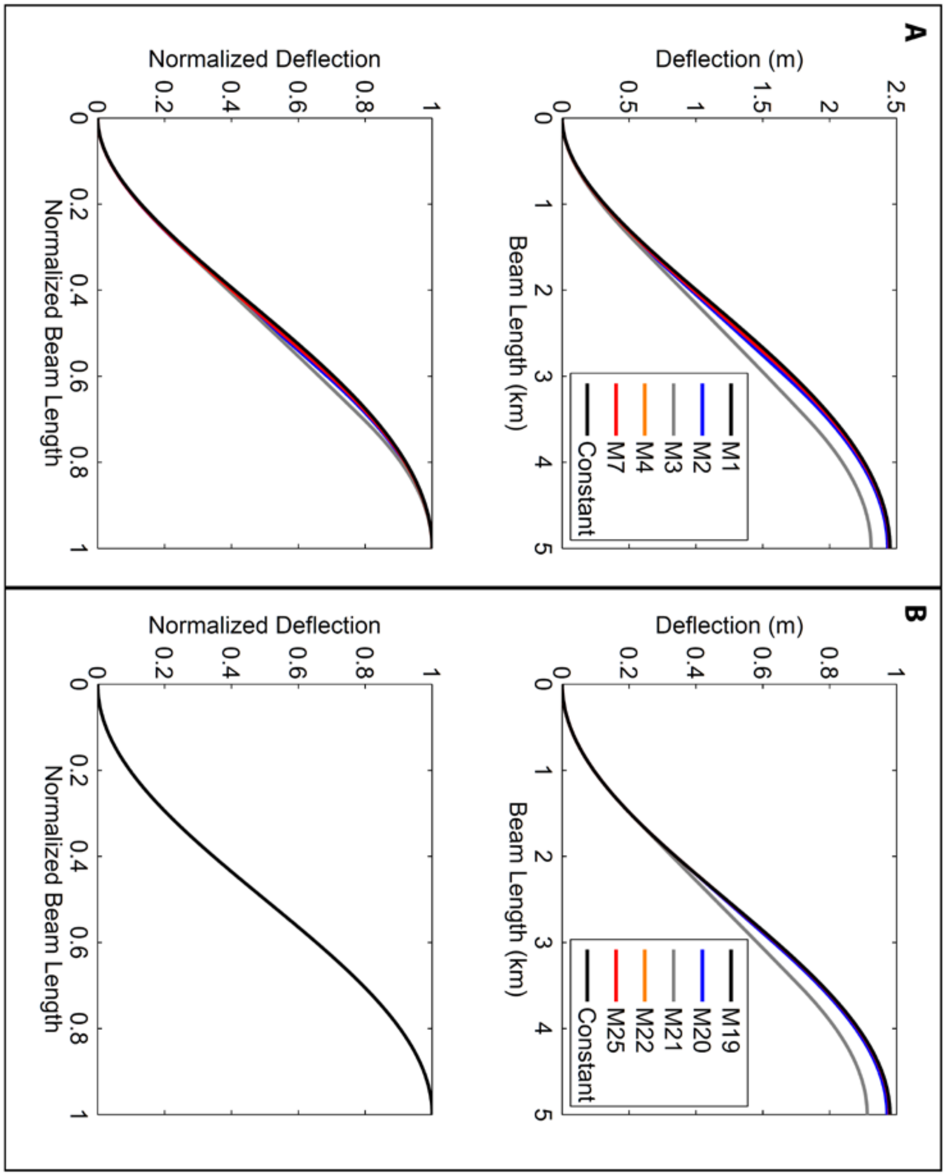

Figure 5B.1: Figures showing the modeled beam deflection for a representative set of moduli profiles. Panel A shows the results for a constant pressure distribution, while panel B shows the results for a linearly varying pressure distribution. The upper plot in each panel is the absolute deflection, while the lower plot is the normalized deflection. In all figures, the black line is the value for a homogenous model. Model numbers correspond to the model names in table B1.

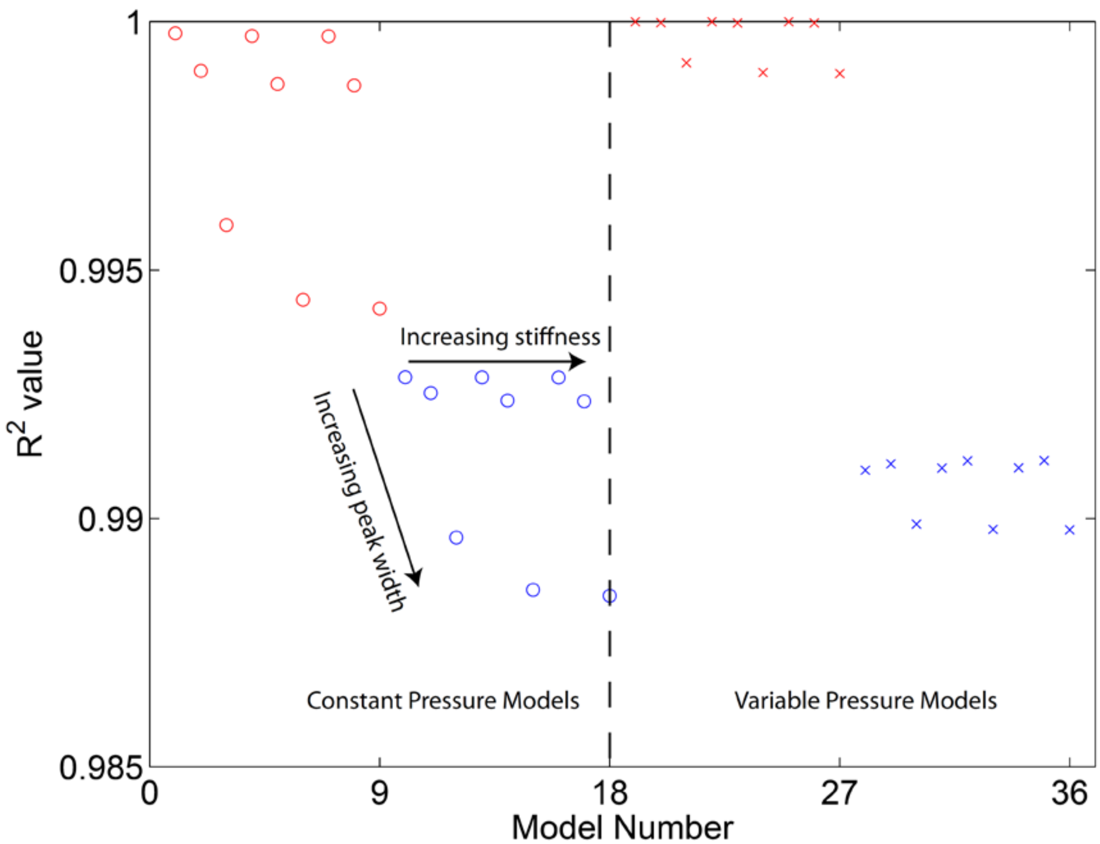

Figure 5B.2: R^2 values comparing the normalized beam deflections for our 36 variable elasticity models to the homogeneous model. The vertical axis is the R^2 value, while the horizontal axis is the model number. Symbols correspond to the loading condition (circles=constant, x's=varying pressure), while the color corresponds to the edge condition (red=constant, blue=varying). All values are very close to an R^2 value of 1.

Name	Peak Width %	Peak Magnitude	Edge Moduli	R^2 (1-18)	R^2 (19-36)
Constant	0	Same	Constant	1	
M1	10	1 order	Constant	0.9998	1
M2	20	1 order	Constant	0.9990	1
M3	40	1 order	Constant	0.9959	0.9992
M4	10	2 orders	Constant	0.9997	1
M5	20	2 orders	Constant	0.9987	1
M6	40	2 orders	Constant	0.9944	0.9990
M7	10	3 orders	Constant	0.9997	1
M8	20	3 orders	Constant	0.9987	1
M9	40	3 orders	Constant	0.9942	0.9990
M10	10	1 order	Linear	0.9928	0.9910
M11	20	1 order	Linear	0.9925	0.9911
M12	40	1 order	Linear	0.9896	0.9899
M13	10	2 orders	Linear	0.9928	0.9910
M14	20	2 orders	Linear	0.9924	0.9912
M15	40	2 orders	Linear	0.9886	0.9898
M16	10	3 orders	Linear	0.9928	0.9910
M17	20	3 orders	Linear	0.9924	0.9912
M18	40	3 orders	Linear	0.9884	0.9898
Models M19-M36 are the same as the above models with a variable applied pressure.					

Table 5B.1: Beam model elasticity profile parameters and R2 values for the 37 models run as part of Appendix B. The peak width defines the percent of the overall peak length that has a raised moduli. The peak magnitude column corresponds to the magnitude of the central modulus relative to the modulus at the edge of the beam. The edge modulus describes the nature of the moduli near the beam edges. The R^2 value is defined in the text of Appendix B. Note the models M19-M36 have the same values as the corresponding models M1-M18, but have a variable applied pressure profile rather than a constant pressure, as described in the main text of Appendix B.

Appendix 5C: Finite Element Output: Spatial Variability of Effective Viscosity

In this appendix, we present figures of the full two-dimensional effective viscosity field for the nonlinear viscoelastic finite element models used to analyze the effect of nonlinearity (subsection 5.3.2). We define the effective viscosity to be a stress-dependent modulus that linearized the viscous component of the material model, as shown below:

$$\eta_{eff} = \frac{1}{A{\sigma_{eff}}^{n-1}} \qquad (5C.1)$$

The five figures correspond to crack lengths of twenty meters, one kilometer, two kilometers, three and a third kilometers, and five kilometers. The twenty meter crack falls into the half-space deformation regime, the one kilometer crack is in the transitional regime, and the remaining models lie within the beam-like regime. In all models, the black line indicates the location and length of the basal crack.

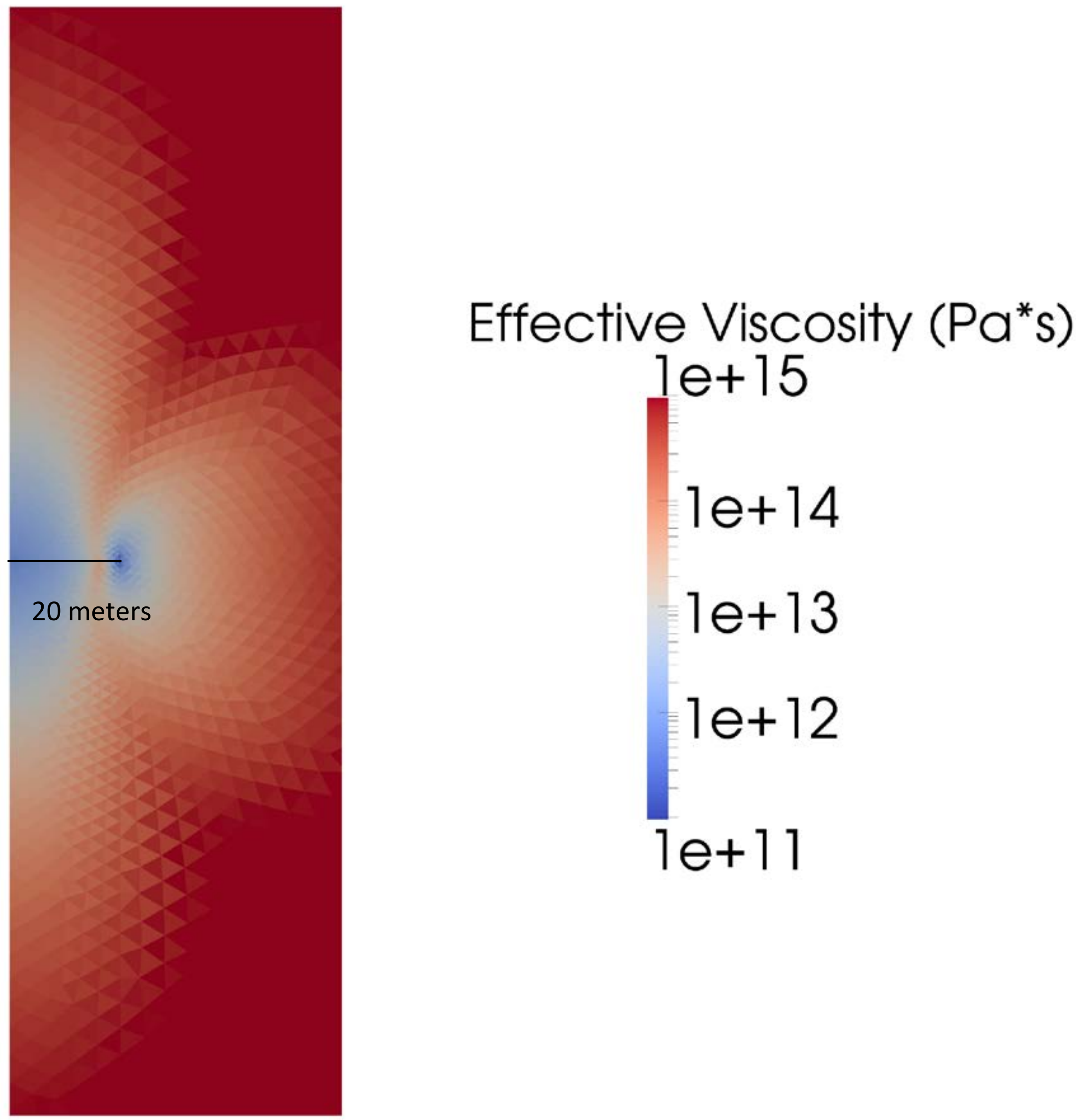

Figure 5C.1: Effective viscosity distribution for a crack 20 meters long. Note that the upper and lower edges of this figure do not correspond to the free surface and bottom of the mesh, respectively. The boundaries are chosen arbitrarily to aid in view of the effective viscosity distribution. This crack length is in the half-space regime.

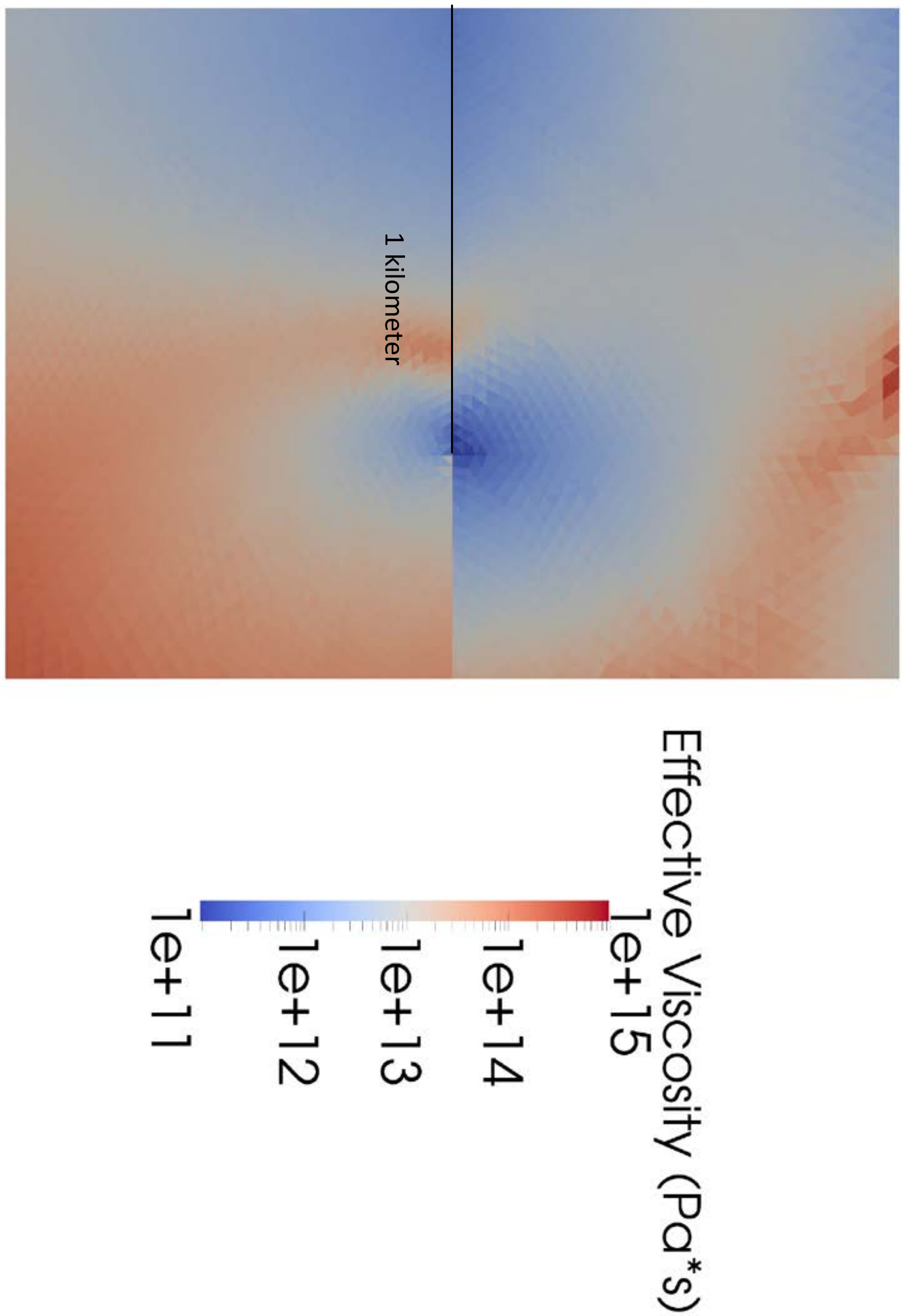

Figure 5C.2: Effective viscosity distribution for a crack one kilometer long. This crack falls within the transitional regime. Note the figure is rotated 90 degrees.

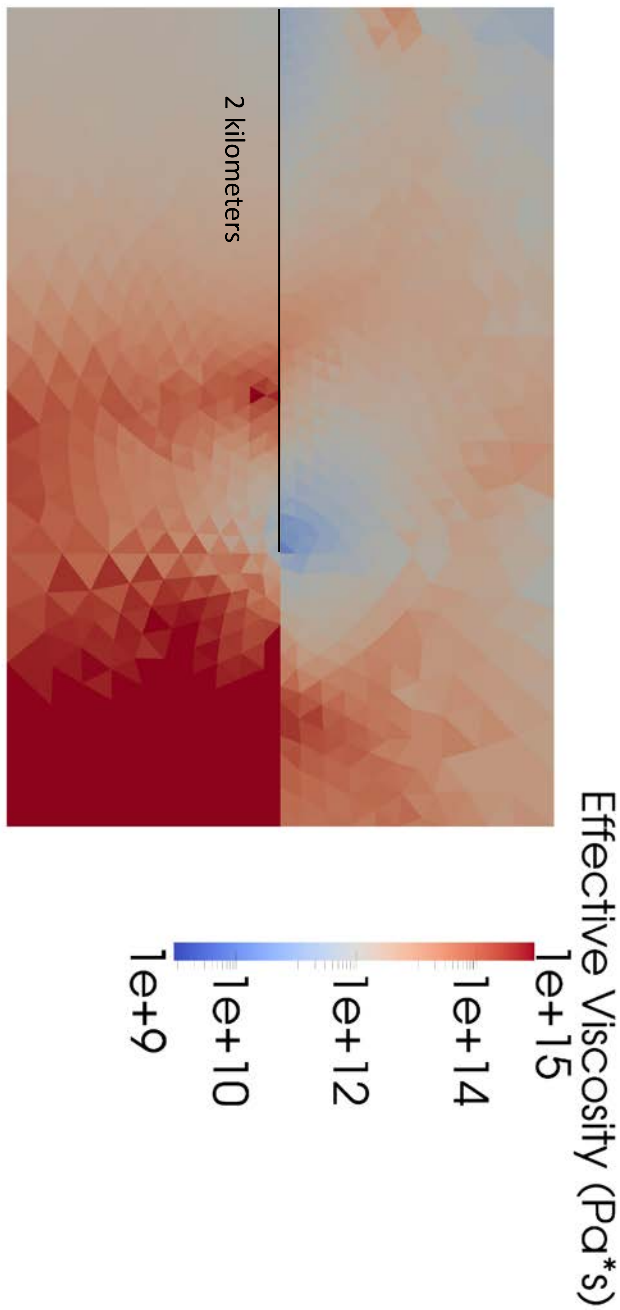

Figure 5C.3: Effective viscosity distribution for a crack two kilometers long. This crack length lies right within the beam-like regime. Note the figure is rotated 90 degrees.

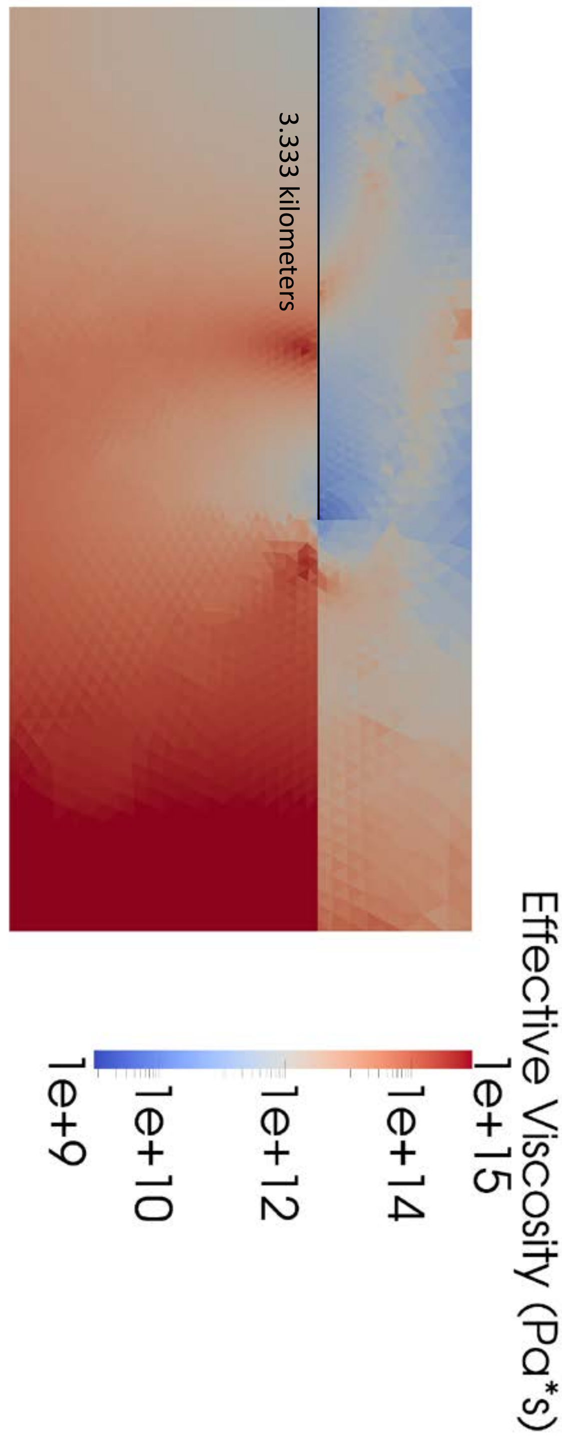

Figure 5C.4: Effective viscosity distribution for a crack 3.333 kilometers long. This crack length lies within the beam-like regime. Note the figure is rotated 90 degrees.

Figure 5C.5: Effective viscosity distribution for a crack five kilometers long. This crack length lies within the beam-like regime. Note the figure is rotated 90 degrees.

Appendix 5D: Conduit Size

In section 5.4, we demonstrate that we can fit the observations of Das et al. (2008) to within a factor of two of the observations; however, as part of this analysis, we need to make an assumption of the value of $\left(\frac{a}{L}\right)$, the ratio of the conduit's long axis to the basal crack length. In this appendix, we discuss the impact of the choice of $\left(\frac{a}{L}\right)$ on our overall solution, and look how well our models predict the observed surficial crack.

We start by looking at the relationship of $\left(\frac{a}{L}\right)$ to the two correction factors χ and χ_w, as defined in equations 5.14 and 5.15. Figure 5D.1 plots the value of these corrections factors, as well as the total correction to pressure, $\chi * \chi_w$, as functions of crack length for several assumed values of $\left(\frac{a}{L}\right)$. In this figure, we take the result from our elastic model for the value of crack opening and drainage volume used to determine these parameters; our choice here is arbitrary and the correction factors follow the same general trends independent of the model rheology. As the crack length increases, the value of χ increases asymptotically towards 1. For χ_w, the value is fixed at 1 until the lake completely drains into the conduit. For some of the models, χ_w will jump above 1 at the onset of the post-drainage phase; this behavior is due to the model over-shooting the total drainage volume, which is then corrected at the next timestep. After the lake completely drains, χ_w rapidly drops and asymptotically approaches 0. From the $\chi * \chi_w$ curve, we see that χ_w dominates the total value of the correction factor once in the post-drainage phase. For the varying values of $\left(\frac{a}{L}\right)$, we see that decreasing the relative conduit size delays the complete lake drainage. The net result is that a smaller overall conduit will result for models with a smaller value of $\left(\frac{a}{L}\right)$, despite the longer crack size L at drainage.

Furthermore, reducing $\left(\frac{a}{L}\right)$ results in a reduced correction factor over the entire crack length. Reducing the correction factor results in a smaller peak value of inlet pressure, p_I, for a given model, which in turn reduces the value of the crack velocity, U_{tip}, as seen in figure 5D.2. In this figure, we see that reducing the size of the conduit has the effect of reducing the overall crack propagation speed until the lake completely drains and the correction factor χ_w "turns on." Once χ_w is a non-one value, the crack velocities all follow the same evolution curve, essentially independent of the conduit size (the velocities vary by less than 1/10% between values of $\left(\frac{a}{L}\right)$). From this relationship, we can make the somewhat surprising statement that once the lake has completely drained, the geometry of the conduit does not influence the further evolution of the basal crack, even though the excess fluid pressure in the conduit is the driver of post-drainage crack growth.

The net results of the variation of the correction factors and the crack propagation velocity with the selection of $\left(\frac{a}{L}\right)$ is summarized in figure 5D.3. As with figure 5.10, this figure shows the drainage volume, drainage rate, and crack opening values as a function of time, though the models shown here have the fluid drag correction added. As expected, we see that reducing the value of $\left(\frac{a}{L}\right)$ causes the duration of the total drainage cycle to increase and the drainage rate to drop due to the reduced crack propagation velocity. Furthermore, the total crack opening drops as the relative conduit size is reduced, due to the reduced magnitude of the correction factors. Following this trend and running models at progressive smaller values of $\left(\frac{a}{L}\right)$ allowed us to find the best-fit model presented in figure 5.11, which has a value of $\left(\frac{a}{L}\right) = 0.51$.

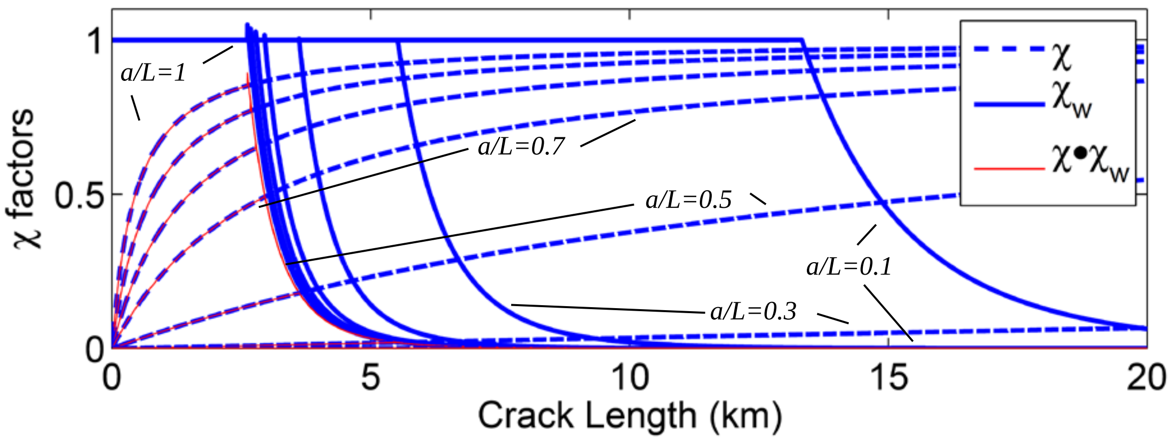

Figure 5D.1: Variation of the corrections factors χ and χ_w with the relative conduit size $\left(\frac{a}{L}\right)$. The dashed line shows χ, the solid line χ_w, and the red line the total correction factor $\chi \cdot \chi_w$. Curves for relative conduit lengths of 1.0, 0.9, 0.8, 0.7, 0.5, 0.3, and 0.1 are shown.

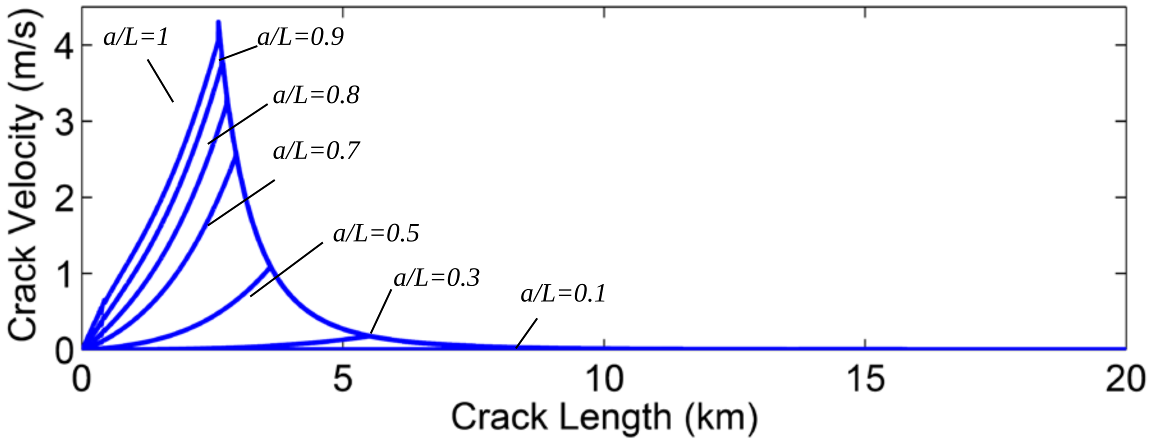

Figure 5D.2: Variation of the crack propagation speed, U_{tip}, as a function of crack length, for a series of relative conduit lengths of $\left(\frac{a}{L}\right)$ equal to 1.0, 0.9, 0.8, 0.7, 0.5, 0.3, and 0.1. Note that the curves all fall on the same line, controlled by the value of χ_w when the surficial lake has completely drained.

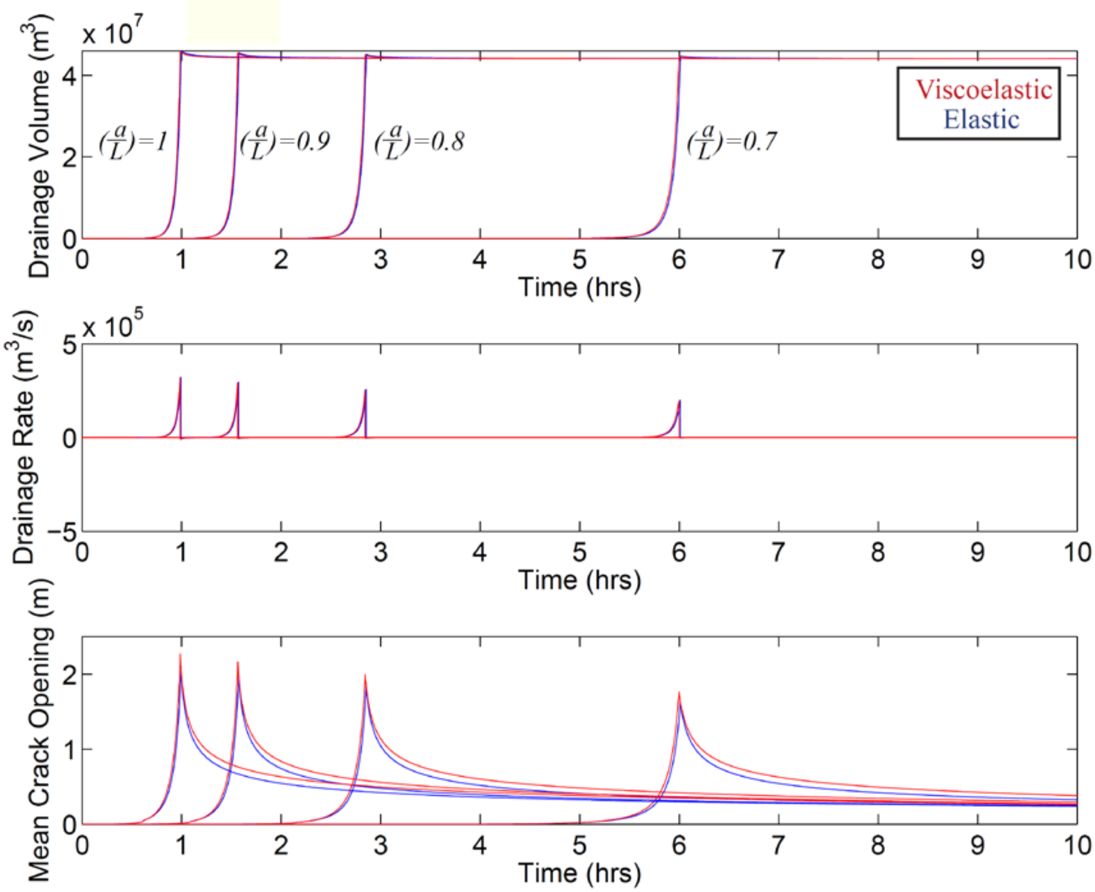

Figure 5D.3: Drainage volumes, drainage rates, and average crack openings for models with a range of $\left(\frac{a}{L}\right)$ values equal to 1.0, 0.9, 0.8, 0.7, for models with the fluid drag correction, as functions of times. The red curves show the viscoelastic results, while the blue curves show the elastic results.

Appendix 5E: Finite Element Output: Surface Deformation Caused by Crack Opening

In subsection 5.4.2, we found the surface deformation that occurs at a location equivalent to the GPS station of Das et al. (2008) by using a finite element model. For these finite element models, we used the two-dimensional mesh geometry shown in figure 5E.1, which models only the glacier above the basal crack. In this model, we only consider the surface deformation due to the presence of the basal crack, and neglect any surface deformation caused by the opening of the drainage conduit. To represent the crack, the displacement profile from our analytic model (either the elastic or linear viscoelastic) is applied to the base of the model, with any displacement beyond the length of the crack set to zero. In these models, the crack is stationary and the crack length does not evolve.

As our assumption is that the vertical drainage conduit is a long, oblate cylinder (see figure 5.9), there must be three-dimensional effects that limit the horizontal motion of the ice at the conduit that are neglected in a two-dimensional model. To bracket this three-dimensional effect, we ran models with two end-member conditions at the conduit. The first condition represents ice near the lateral ends of the conduit. For this condition, we force the horizontal displacement to always be equal to zero (i.e., there is symmetry across the conduit). The second condition represents ice near the lateral center of the conduit, where the ice on either side of the conduit is horizontally decoupled. For this location, we allow the mesh at the conduit to deform freely. The resulting difference in the displacements at the GPS location 1.7 kilometers away is small, with the peak horizontal and vertical deformations being less than a factor of two different for these models, as demonstrated by the displacement profiles for the models shown in figures 5E.2 and 5E.3. The figures in the main paper (i.e., figures 5.12 and 5.13) show results from models assuming the GPS station is along the centerline of the conduit, as is the case in the survey of Das et al. (2008).

Lastly, the ice in this model is assumed to be elastic. For the models using the elastic crack opening to calculate surface displacement, such an assumption is consistent. However, this approach is clearly not self-consistent when the linear viscoelastic crack opening is used, as in this formulation the viscous and elastic crack opening are assumed to only act elastically on the deformation of the glacier (i.e., there is no time-dependent deformation in the glacier). The assumption of elastic deformation is a necessary simplification, as to fully capture the viscous deformation of the glacier, the crack would have to be iteratively lengthened, an approach beyond the scope of this chapter. Thus, the surface displacements for the viscoelastic model (such as are shown in figures 5.12 and 5.13) are only approximately correct, and are underestimate of the total surface deformation. However, using the relative magnitudes of the viscous and elastic crack openings as a guide (figure 5.7A), the expected error is about 10% at most, with shorter cracks having smaller errors than the longer cracks.

Lastly, as we are using finite element analysis, we have the full displacement field over the entirety of our mesh, not just at the location of the GPS station. Figures 5E.4 and 5E.5 show snapshots of the deformation of the glacier at a series of timesteps used in subsection 5.4.2. These figures provide a picture of the full deformation pattern due to the growth of a basal ice crack.

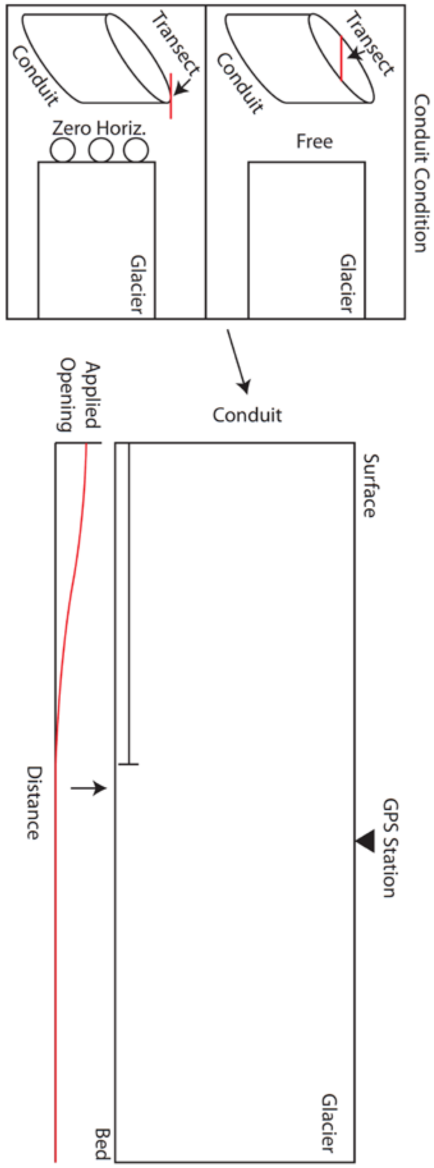

Figure 5E.1: Finite element model setup discussed in appendix 5E. The right portion of the figure shows the mesh, with a defined crack length of *L*, the vertical conduit, and the GPS station location. The two conduit conditions are shown in the left portion of the figure. In each panel, the left portion shows the theoretical two-dimensional transect of the drainage conduit the finite element boundary condition shown on the right of the panel corresponds to.

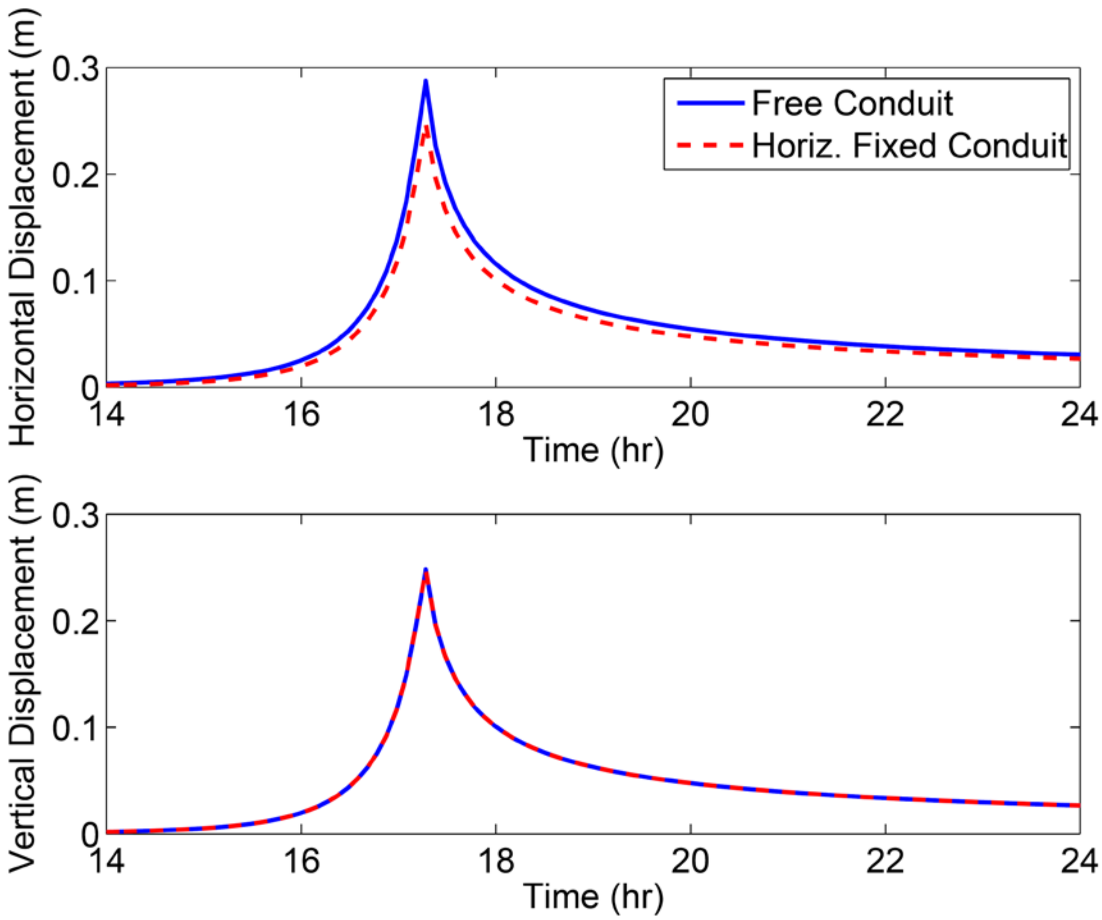

Figure 5E.2: Horizontal and vertical surface deformation for models using the free conduit condition (blue) and the horizontally fixed conduit condition (dashed red). The model shown here is for the elastic crack opening.

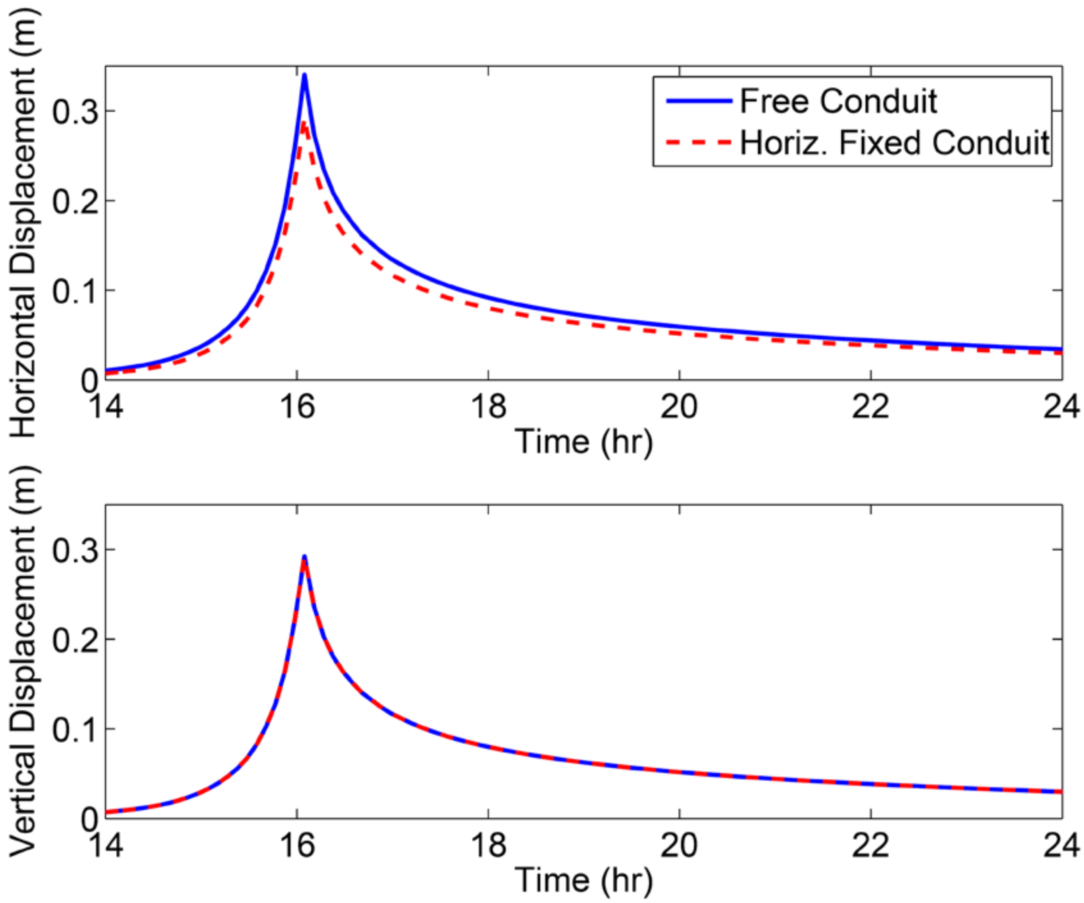

Figure 5E.3: Horizontal and vertical surface deformation for models using the free conduit condition (blue) and the horizontally fixed conduit condition (dashed red). The model shown here is for the viscoelastic crack opening.

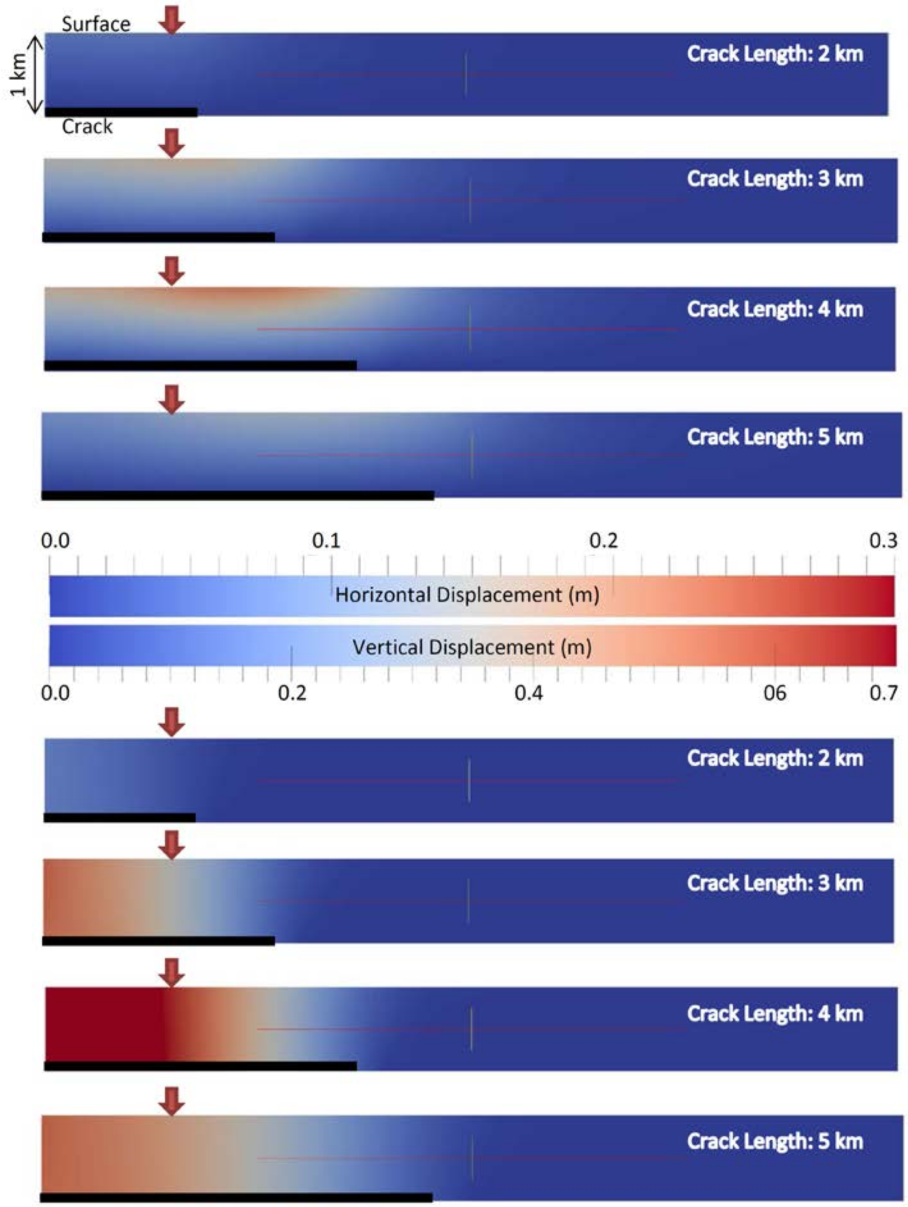

Figure 5E.4: Displacement fields with crack lengths of 2, 3, 4, and 5 kilometers for the finite element models described in subsection 5.4.2 with the elastic value of crack opening. The upper figures are the horizontal displacements, while the lower figures are the vertical displacements. The arrow shows the location of the point approximating the GPS station at 1.7 kilometers away from the crack center (left edge of the domain).

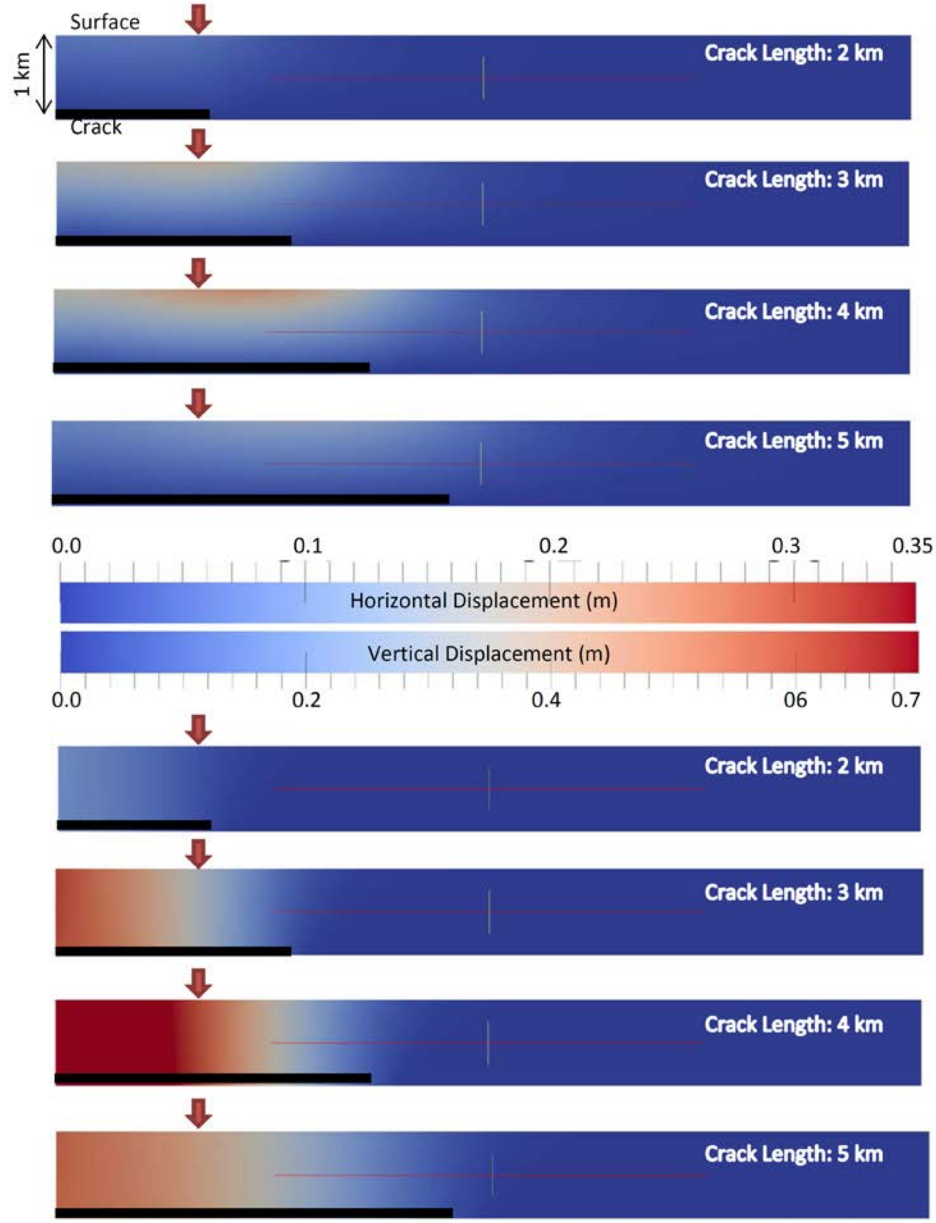

Figure 5E.5: Displacement fields with crack lengths of 2, 3, 4, and 5 kilometers for the finite element models described in subsection 5.4.2 with the viscoelastic value of crack opening. The upper figures are the horizontal displacements, while the lower figures are the vertical displacements. The arrow shows the location of the point approximating the GPS station at 1.7 kilometers away from the crack center (left edge of the domain).